ACS APPLIED MATERIALS & INTERFACES

www.acsami.org

Research Article

# Copper-Epigallocatechin Gallate Enhances Therapeutic Effects of 3D-Printed Dermal Scaffolds in Mitigating Diabetic Wound Scarring

Yanke Hu,[‖] Yahui Xiong,[‖] Yongkang Zhu,[‖] Fei Zhou, Xiaogang Liu, Shuying Chen, Zhanpeng Li, Shaohai Qi,* and Lei Chen*

Cite This: *ACS Appl. Mater. Interfaces* 2023, 15, 38230−38246

Read Online

ACCESS | Metrics & More | Article Recommendations | Supporting Information

**ABSTRACT:** Morbid dermal templates, microangiopathy, and abnormal inflammation are the three most critical reasons for the scarred healing and the high recurrence rate of diabetic wounds. In this present study, a combination of a methacrylated decellularized extracellular matrix (ECMMA, aka EM)-based hydrogel system loaded with copper-epigallocatechin gallate (Cu-EGCG) capsules is proposed to fabricate bio-printed dermal scaffolds for diabetic wound treatment. Copper ions act as a bioactive element for promoting angiogenesis, and EGCG can inhibit inflammation on the wound site. In addition to the above activities, EM/Cu-EGCG (E/C) dermal scaffolds can also provide optimized templates and nutrient exchange space for guiding the orderly deposition and remodeling of ECM. In vitro experiments have shown that the E/C hydrogel can promote angiogenesis and inhibit the polarization of macrophages to the M1 pro-inflammatory phenotype. In the full-thickness skin defect model of diabetic rats, the E/C dermal scaffold combined with split-thickness skin graft transplantation can alleviate pathological scarring via promoting angiogenesis and driving macrophage polarization to the anti-inflammatory M2 phenotype. These may be attributed to the scaffold-actuated expression of angiogenesis-related genes in the HIF-1$\alpha$/vascular endothelial growth factor pathway and decreased expression of inflammation-related genes in the TNF-$\alpha$/NF-$\kappa$B/MMP9 pathway. The results of this study show that the E/C dermal scaffold could serve as a promising artificial dermal analogue for solving the problems of delayed wound healing and reulceration of diabetic wounds.

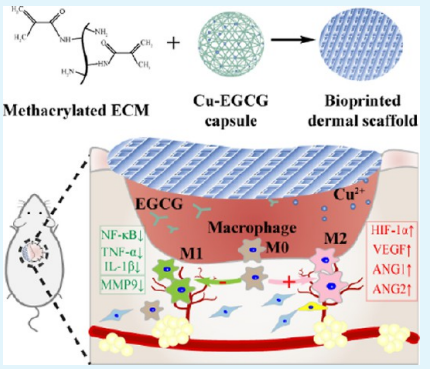


**KEYWORDS:** *metal-polyphenol capsule, extracellular matrix, split-thickness skin graft, diabetic wound healing, in situ tissue regeneration*

## 1. INTRODUCTION

Wounds compromise the integrity of the skin and affect its erect barrier to bacterial invasion and other possible environmental hazards.[1] Besides venous leg ulcers and pressure ulcers, diabetic wounds are one of the most challenging tasks for wound care professionals, with diabetic foot ulcers (DFUs) representing the most common manifestation of diabetic wounds.[2] In 2021, there were approximately 536.6 million individuals between the ages of 20 and 79 worldwide diagnosed with diabetes.[3] The lifetime incidence of DFUs may be as high as 25%.[4] Diabetic patients often struggle with wound healing after skin injury due to pathological hyperglycemia, reduced nerve sensitivity, and impaired circulation in peripheral arteries.[4,5] The morbid dermal template is a common characteristic of these wounds, contributing to disrupted angiogenesis and collagen deposition. It overlaps with the uncontrolled inflammatory reaction, leading to delayed wound healing, scar formation, and high recurrence rates.[5−7] These complications not only bring a heavy economic burden to patients and society but also lead to serious consequences such as amputation or even death (mortality rate of 40−59% 5 years after amputation).[8] It is estimated that the annual cost related to DFUs amounts to $9−13 billion in excess of diabetes-related costs in the US.[9] The annual cost of DFU treatment in Europe is reported to be as high as 10 billion euros.[10] How to quickly replenish the wound with a high-quality extracellular matrix (ECM) while solving the inflammatory imbalance and microcirculation disorder of the diabetic wound so that the wound can heal quickly and efficiently is a key problem that needs to be solved urgently.

The acellular dermal matrix (ADM) is a biological material that removes the cellular components in the skin by physical, chemical, or biological methods and retains the dermal matrix and three-dimensional space frame structure. Among various materials used for diabetic wound repair, the ADM has high water retention capacity and exhibits certain resistance to protease degradation. Its therapeutic effects have been recognized and approved by professional wound repair guidelines and consensus.[11] For possessing similar ECM

Received: April 3, 2023
Accepted: July 10, 2023
Published: August 3, 2023

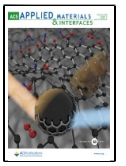

**Scheme 1. ECMMA, aka EM, and Cu-EGCG Capsules Were Combined to Prepare E/C Bioink, and Then the E/C Dermal Scaffold Was Made by Extruded Bioprinting**[a]

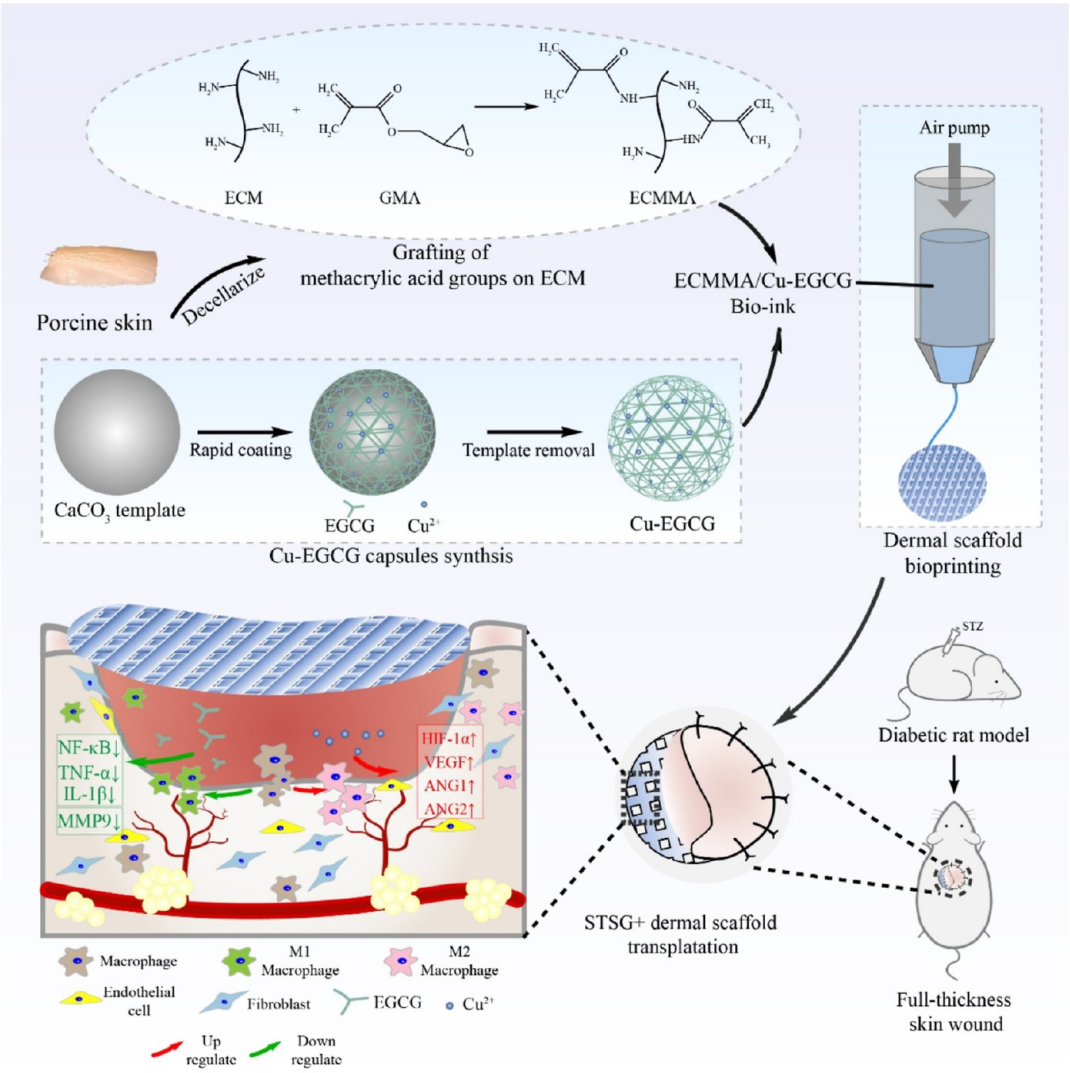


[a]In the full-thickness skin defect model of diabetic rats, the E/C dermal scaffold combined with STSG transplantation can promote dermal regeneration and angiogenesis and promote macrophage polarization to the M2 anti-inflammatory phenotype.

components to normal skin, the ADM can mobilize the inherent regeneration potential of the injured area and drive wound healing, which makes it an ideal "template" for inducing wound regeneration.[12−14] But the dense fiber structure makes it difficult for cells to enter smoothly and carry out matrix deposition and remodeling. Besides, the ability to regulate inflammation and induce vascularization is limited, which make it difficult to achieve satisfactory results when the ADM is applied to diabetic wounds.[15]

Human-derived allogeneic ADMs are in short supply and cannot meet clinical demands. Porcine ADM, on the other hand, exhibits similar composition, immunoreactivity, and anatomical structure to that of humans, along with low immunogenicity, making it a highly regarded option.[16,17] However, the arrangement of its internal fibers is excessively dense, leading to poor nutrient permeability and making it difficult for re-cellularization and re-vascularization. This leads to a low graft survival rate. Therefore, it can only be used as a temporary dressing. 3D printing technology can help researchers to precisely manufacture materials based on optimally designed structures and active ingredient formula composition, enabling the creation of artificial substances that are more flexible and tailored for accurate therapeutic purposes.[18,19] Girardeau-Hubert et al.[20] demonstrated in vitro that 3D-printed decellularized ECM (dECM)-based skin analogues can promote the response of epidermal-forming cells and fibroblasts to the microenvironment compared with type I collagen-based skin analogues. Chen et al.[21] used 3D printing to prepare dermal analogues with pore sizes similar to those of the human dermal matrix, which significantly improved the appearance of healing and reduced scar contraction in vivo compared with commercial dermal matrix materials (Pelnac) and split-thickness skin graft (STSG). In summary, 3D-printed ECM-based dermal scaffolds provide an excellent strategy for in situ tissue regeneration and repair of skin injuries, which can drive the body's own repair ability more efficiently and improve the quality of wound healing. However, for the treatment of diabetic wounds with an abnormal inflammatory microenvironment and blood supply,


https://doi.org/10.1021/acsami.3c04733
ACS Appl. Mater. Interfaces 2023, 15, 38230−38246

3D-printed dermal analogues should be improved in anti-inflammatory and pro-angiogenic efficiency.

EGCG, the active ingredient in green tea, has been recognized by the FDA to have anti-inflammatory, antioxidant, antimicrobial, and other biological properties. Studies have shown that EGCG can exert anti-osteoarthritis effects by reducing ECM degradation, cartilage inflammation, and cell senescence and improve wound healing in diabetic mice by inhibiting macrophage aggregation and the inflammatory response.[22,23] But the easy oxidation of EGCG limits its application.[24] The metal−polyphenol network is a supramolecular amorphous network formed by the coordination interaction between multivalent metal ions and polyphenols, which combines the properties of metal ions and polyphenols. It is widely used in the biomedical field because of its physiological stability, good biodegradability, biosafety, and a variety of functions.[25] Copper ions have been shown to be effective in promoting angiogenesis and inducing vascular endothelial growth factor (VEGF) secretion. Duan et al.[26] prepared copper-epigallocatechin gallate (Cu-EGCG) capsules, which combined the therapeutic anti-inflammatory and antioxidant activities of EGCG and the angiogenic activity of copper ions. VEGF secretion in ischemic lower extremities in rats was induced by Cu-EGCG injection, which significantly improved the blood supply of ischemic lower extremities in rats. The introduction of Cu-EGCG could significantly improve the usability and biological characteristics of the material.

In this study, we developed a multifunctional hydrogel that can efficiently address the issues of diabetic wound scarring and reulceration. The hydrogel consists of Cu-EGCG and methacrylated dECM, and we conducted in vitro tests to assess its physical properties, bio-compatibility, pro-angiogenic effect, and anti-inflammatory effects. Based on our findings, we developed a novel 3D-printed dermal scaffold called methacrylated decellularized extracellular matrix (ECMMA, aka EM)/Cu-EGCG (E/C) that resembles the porous structure of the natural human dermal matrix. Our E/C scaffolds were proved to be highly effective in facilitating the therapeutic effects of STSG by offering high-quality ECM, an ideal regenerative microenvironment for repair cell ingrowth, curtailing inflammation, and promoting angiogenesis. Our results suggest that EGCG-empowered dermal implants can provide a transformable solution to diabetic wound care, improving the inflammatory imbalance and microcirculation issues (Scheme 1).

## 2. EXPERIMENTAL SECTION

**2.1. dECM Preparation and Detection.** Porcine skin was sourced commercially. The porcine skin was decellularized according to the method of Kim et al.[16] Briefly, the porcine dermis was removed from the epidermis and subcutaneous tissue and cut into 1 cm × 1 cm blocks. The tissues were incubated successively with 0.25 wt % trypsin mixed with 1 mM ethylene glycol, PBS solution mixed with 1 mM ethylene diamine tetraacetic acid (EDTA) and 1 wt % Triton-X-100, and 30 U/mL DNase solution containing 10 mM $MgCl_2$ to remove cell components and fat. After freeze drying, porcine dECM was made.

Porcine natural skin (NS) and dECM were formalin-fixed and paraffin-embedded for sectioning. Sections were stained with hematoxylin and eosin (H&E) to observe the structural changes, with DAPI for staining of the nuclei and with Masson trichrome reagent to measure collagen. The DNA content of NS and dECM was separated and quantitatively determined by agarose gel electrophoresis. The collagen and glycosaminoglycan (GAG) contents were quantified by a hydroxyproline kit (Jiancheng, China) and Blyscan GAG Assay Kit (Biocolor, UK), respectively.

**2.2. Synthesis of Cu-EGCG Capsules.** Cu-EGCG capsules were synthesized according to the previously published literature.[26] Briefly, poly(sodium 4-styrenesulfonate) was dissolved in 20 mM $CaCl_2$ and 20 mM $Na_2CO_3$ at a concentration of 1 mg/mL. The two solutions were quickly mixed with 10 mL each and stirred violently for 30 s. $CaCO_3$ particles were then collected by centrifugation at 10 000 rpm for 5 min and rinsed with deionized water. The suspension was mixed with EGCG (0.5 mL, 24 mM) and $CuCl_2$ (0.5 mL, 24 mM) aqueous solutions. Then, 5 mL of 3-(*N*-morpholino)propanesulfonic acid buffer (100 mM, 20.9 g/L, pH = 8.0) was added. Finally, the resulting particles were washed with deionized water, and $CaCO_3$ particles coated with one Cu-EGCG layer were obtained. The above coating process was repeated 3 times to harvest $CaCO_3$ particles coated with three Cu-EGCG layers. The Cu-EGCG capsule was obtained by incubating particles from the previous step into the EDTA solution (200 mM, pH = 8) to remove the $CaCO_3$ templates. The morphological structure of Cu-EGCG particles was observed using transmission electron microscopy (TEM; H800, Hitachi, Japan, 100 kV). The elemental distribution of Cu-EGCG was determined by energy-dispersive X-ray spectroscopy (EDS).

**2.3. Preparation of EM and the E/C Hydrogel.** The dECM was dissolved in pepsin acetic acid solution and titrated to neutral pH with 1 M NaOH. Then, the solution was incubated overnight with glycidyl methacrylate (GMA). After dialysis at 37 °C for 3 days to remove uncrosslinked GMA, the solution was lyophilized to form EM. Different amounts (10, 15, and 20%; wt/v) of EM were added to the solution containing 0.1% LAP (wt/v) to prepare 10, 15, and 20% EM hydrogels. Cu-EGCG capsules were added to the EM hydrogel at concentrations of 25, 50, 100, and 200 $\mu$g/mL to make the E/C hydrogel. Finally, the hydrogels were polymerized via exposure to 350 nm UV light for 20 s.

**2.4. Characterization.** The chemical structures of dECM and EM were detected by $^1$H nuclear magnetic resonance spectroscopy ($^1$H NMR). The functional groups of dECM and EM were detected by Fourier transform infrared spectroscopy (FTIR, Vertex-70, Bruker, Germany). Scanning electron microscopy (SEM) (S-3400, Hitachi, Japan) was used to obtain microscopic morphology images of the lyophilized EM hydrogel at an accelerating potential of 5 kV. The pore size was analyzed using Nano Measurer software. For porosity, the weight of the lyophilized hydrogel was measured and recorded as M1. The hydrogel was then immersed in anhydrous ethanol until it reached saturation, and excess ethanol was removed by gently pressing filter paper against both sides of the sample for 30 s. The sample was quickly reweighed and recorded as M2. The porosity of the sample was calculated as follows

$$\text{porosity ratio } (\%) = (\text{M2} - \text{M1})/(\rho \times V) \times 100$$

In this formula, $\rho$ represents the density of anhydrous ethanol, which is 0.79 g/cm$^3$ and $V$ represents the volume of the scaffold being tested (cm$^3$).

**2.5. Swelling Ratio Analysis.** Swelling experiments were conducted according to the gravimetric method reported previously.[27] Briefly, the hydrogel samples were weighed, and the initial weight was recorded as $W_0$. Subsequently, they were immersed in PBS solution at 37 °C and retrieved at certain time points (1, 2, 3, 4, 5, and 6 h). The moisture on the surface of the hydrogels was gently absorbed by filter paper and weighed immediately, which was recorded as the swelling weight ($W_t$). The swelling ratio of the hydrogels was calculated using the following formula

$$\text{swelling ratio } (\%) = (W_t - W_0)/W_0 \times 100$$

**2.6. Compression Tests.** We measured the deformability of EM hydrogels by a universal testing machine (Electroforce3220; Bose, USA). The hydrogel was placed in a compression sensor and compressed at a rate of 0.05 mm/s to 60% to obtain a stress/strain curve.



https://doi.org/10.1021/acsami.3c04733
ACS Appl. Mater. Interfaces 2023, 15, 38230−38246

**2.7. Rheological Assessment.** The rheological behavior of the hydrogels was tested using a TA rheometer (Kinexus, Malvern Instruments, UK). In our study, a stainless steel parallel plate rotor (25 mm) was used to perform dynamic strain scanning from 0.1 to 10 rad/s at 25 °C. The storage modulus ($G'$) and loss modulus ($G''$) were obtained by subsequent calculation.

**2.8. Degradation of EM In Vitro.** The biodegradation performance of the hydrogel was determined by enzymatic degradation experiments. Briefly, the hydrogel samples were incubated in PBS with or without 100 U/mL lysozyme at 37 °C and 70 rpm. After incubating for a certain time, the hydrogels were removed, rinsed, lyophilized, and weighed. The degradation rate was calculated by the following formula

$$\text{weight loss rate } (\%) = (W_0 - W_t)/W_0 \times 100$$

In this formula, $W_0$ refers to the original dry weight of the lyophilized hydrogel and $W_t$ refers to the dry weight of the lyophilized hydrogel at the designated time.

**2.9. In Vitro $Cu^{2+}$ Release Kinetics.** $Cu^{2+}$ release in vitro was detected by inductively coupled plasma atomic emission spectroscopy (ICP−AES). Briefly, 1 mL of the E/C hydrogel was incubated in 4 mL of PBS solution and shaken (150 rpm, 37 °C) for 3 days. At various time points, 1 mL of the supernatant was taken and supplemented by adding an equal volume of PBS solution. The concentration of $Cu^{2+}$ was measured by ICP−AES. The cumulative $Cu^{2+}$ release rate was then calculated.

**2.10. 3D Bioprinting of EM and E/C Dermal Scaffolds.** Bioprinting was carried out in an extrusion bioprinting system custom-made by our team. The printing process was kept sterile. The printing parameters were set as follows: ambient temperature (18 °C), 4 °C printing platform, 30 °C printing head, 100 μm inner diameter of the nozzle, 0.1−0.3 MPa air pump pressure, and 10 mm/s moving speed of the nozzle. The dermal scaffolds were printed in 4 layers with a single layer size of 20 mm × 20 mm. The UV light time was 20 s.

**2.11. Biocompatibility Tests In Vitro.** *2.11.1. Cell Viability Assay.* The hydrogels were immersed in complete endothelial cell medium [basal medium + 5% fetal bovine serum (FBS) + 1% ECGS+ 0.2% Normocin] at a ratio of 10% (v/v) and incubated at 37 °C for 72 h on a shaker for leaching. The culture media of different groups were as follows: NC: complete endothelial cell medium; EM group: EM hydrogel extract; E/C25 to E/C200 group: E/C hydrogel with Cu-EGCG concentrations of 25, 50, 100, and 200 μg/mL. The cytotoxicity of hydrogels for human microvascular endothelial cells HMEC-1 (Meisen, CTCC-001-0219) was evaluated by CCK-8 assay. HMEC-1 cells were cultured in 96-well plates at a seeding concentration of 2000 cells/well for 6 h, and then the culture medium was replaced according to different groups. After incubation for 24, 48, and 72 h, 10 μL of CCK8 solution was added to each well. The optical density was measured on a Multiskan Sky Microplate Spectrophotometer (Thermo Scientific, USA) at 450 nm.

*2.11.2. Live/Dead Staining.* One hundred microliters of the hydrogel solution was added dropwise into a confocal culture dish (Ibidi, 81218-200), cross-linked with UV light for 20 s, and seeded with HMEC-1 cells on the surface. After 24, 48, and 72 h of culture, the medium was replaced by Calcein AM/PI detection working solution (Beyotime, China) and incubated at 37 °C in the dark for 30 min. Then, the samples were observed under an Olympus FV3000 fluorescence microscope (Olympus, Japan).

*2.11.3. Cytoskeleton Staining.* HMEC-1 cells were seeded on the surface of the hydrogels according to the above steps. After culturing for 24, 48, and 72 h, the medium was aspirated, and the hydrogels were rinsed with PBS and fixed with 4% paraformaldehyde for 30 min. Then, the cells were soaked in 0.1% Triton X-100 to increase membrane permeability for 10 min. After washing 3 times with PBS solution, the cells were stained with rhodamine-labeled TRITC phalloidin (Invitrogen, USA) for 30 min. The nuclei were stained with DAPI. The samples were observed under a fluorescence microscope.

*2.11.4. In Vitro Tube-Formation Assay.* Tube formation assays were performed on Matrigel-coated 96-well plates. HMEC-1 cells were resuspended in endothelial cell medium and seeded (15 000 cells/well) on Matrigel. After 30 min of incubation, the supernatant was replaced by extracts of various hydrogel groups. The images were taken after 4 h and analyzed utilizing the plugin (Angiogenesis Analyzer) of ImageJ software to calculate the number of junctions and the total length of tubes.

*2.11.5. Scratch Test.* For wound closure/scratch assays, HMEC-1 cells were seeded in a 2-chamber culture insert (Ibidi, USA) in a 24-well plate, and HMEC-1 cells in the logarithmic growth phase were inoculated in the Ibidi chamber. The insert was removed when the cells covered the bottom of each well, which formed a regular ∼500 μm wide gap on the bottom of the well. Cell debris and medium were removed after rinsing with PBS. The hydrogel extracts were added into the wells. Images were taken at predetermined time points, and the wound area was analyzed using ImageJ software.

*2.11.6. Invasion Assay.* The effect of hydrogels on the invasion of HMEC-1 cells was determined by invasion assay as previously described. Briefly, HEMC-1 cells were resuspended in serum-free medium. A total of $5 \times 10^4$ cells were seeded onto the upper chamber with a Matrigel-coated membrane (24-well, 8 μm, BD, USA). The bottom chamber was filled with hydrogel extracts as the chemoattractant. After incubating at 37 °C for 12 h, the surface of the upper chamber was carefully scraped with a cotton swab. The chamber was fixed with methanol, stained with 0.1% crystal violet, and observed under a microscope.

*2.11.7. Polarization of Macrophages In Vitro.* Macrophage polarization was induced in vitro as previously reported.[28] Untreated RAW264.7 cells (labeled M0 macrophages) were seeded in 6-well plates in medium containing DMEM supplemented with 10% FBS overnight. To evaluate the effect of hydrogels on macrophage polarization, 100 ng/mL lipopolysaccharide (LPS) was then added to the culture medium. The hydrogels were coated in Transwell chambers (6-well, 8 μm, BD, USA) and cocultured with the cells for an additional 48 h.

*2.11.8. In Vitro ROS Scavenging Assay.* Intracellular reactive oxygen species (ROS) were evaluated using 2′,7′-dichlorodihydrofluorescein diacetate (DCFDA) staining. Briefly, RAW264.7 cells were cultured in medium containing 1 mM $H_2O_2$ and cocultured with EM hydrogels and E/C hydrogels. After 24 h of incubation at 37 °C, the cells were washed with PBS and incubated with DCFDA (Abcam, USA) for 30 min at 37 °C in the dark. After removing DCFDA, intracellular ROS were observed under a fluorescence microscope.

*2.11.9. Quantitative Real-Time Polymerase Chain Reaction.* Total cellular RNA was extracted using standard TRIzol RNA extraction. cDNA was synthesized using the Servicebio RT First Strand cDNA Synthesis Kit (Servicebio, China). Quantitative real-time polymerase chain reaction (RT-PCR) was performed using SYBR Green Master Mix (Thermo Fisher, USA) following the manufacturer's instructions in a StepOnePlus Real-Time PCR System. Data were analyzed using StepOne V2.0 software (Applied Biosystems). The involved forward and reverse primers are shown in Table S1 in the Supporting Information. The relative expression levels of genes were normalized using GAPDH, and the results were processed by the ΔΔCT method.

**2.12. In Vivo Evaluation of Wound Healing in Diabetic Rats.** *2.12.1. Construction of a Full-Thickness Skin Wound Model in Diabetic Rats.* All animal experiments were reviewed and approved by the Animal Ethics Committee for Clinical Research and Animal Trials of the First Affiliated Hospital of Sun Yat-sen University (approval no. [2023]042). Male SD rats (200−250 g) were given an intraperitoneal injection of 65 mg/kg streptozotocin. Then, the rats with a random blood glucose higher than 16.7 mmol/L were considered diabetic and randomized into four groups ($n$ = 20 per group). The rats were anesthetized with pentobarbital sodium (45 mg/kg body weight). The dorsal and inguinal skin of the rats was prepared and sterilized with povidone iodine and 70% ethanol. A circular full-thickness skin wound (20 mm diameter) was made on each operation site. The subcutaneous fat, blood vessels, and fascia of the obtained inguinal skin pieces were removed as much as possible to obtain an STSG. According to the subsequent treatments of the dorsal wounds, the rats were divided into 4 groups: STSG transplantation (NC), Pelnac


https://doi.org/10.1021/acsami.3c04733
ACS Appl. Mater. Interfaces 2023, 15, 38230−38246

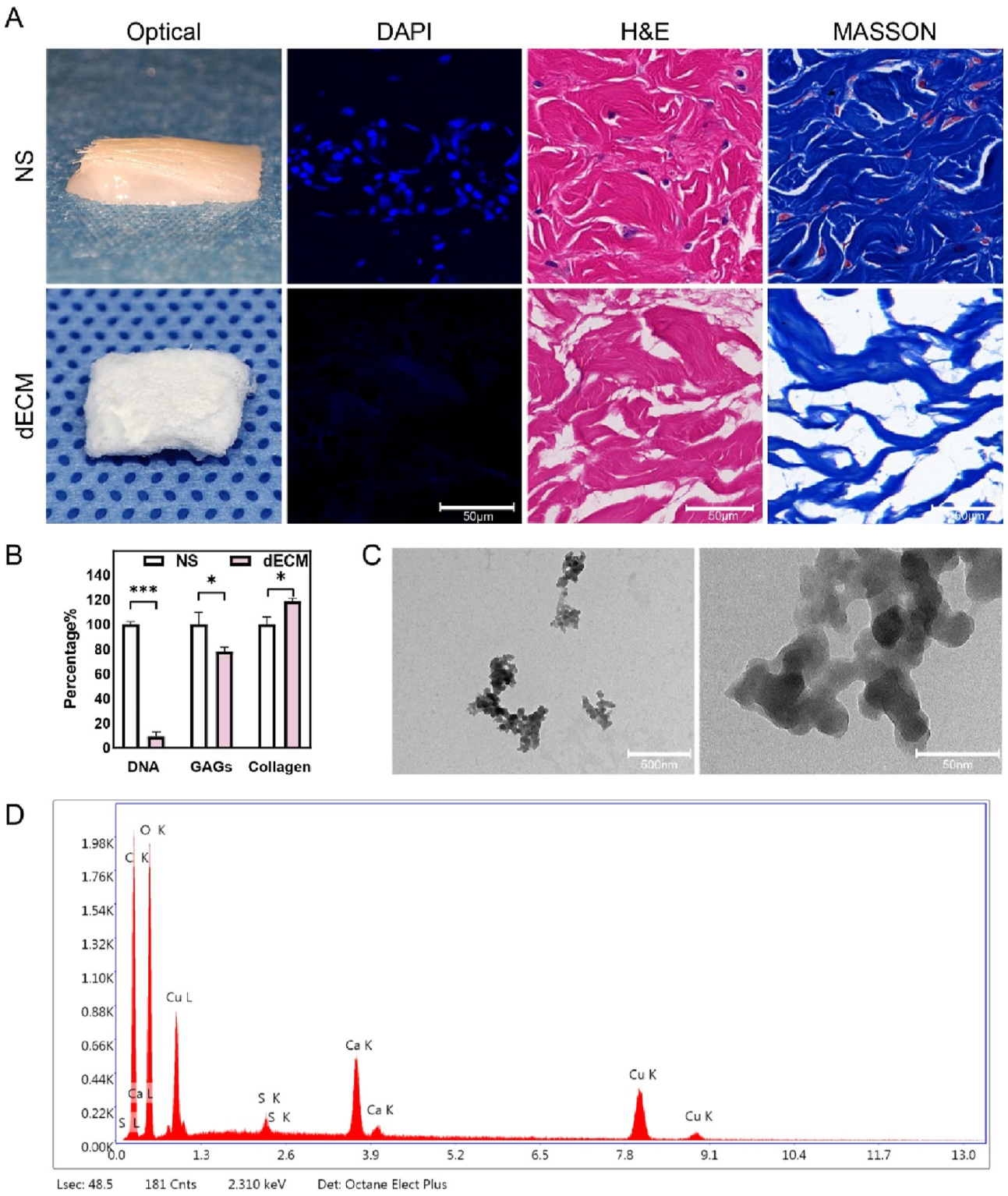


**Figure 1.** Porcine dECM biochemical detection and Cu-EGCG detection. (A) Optical photos and microphotographs of DAPI, H&E, and Masson staining of porcine NS and dECM. (B) DNA, GAG, and collagen content of NS and dECM. (C) TEM images of Cu-EGCG. (D) EDS element mapping images of Cu-EGCG. (*$P$ < 0.05, ***$P$ < 0.001.)

Dermal Substitute (single layer, Gunze, Japan) + STSG transplantation (PL), EM dermal scaffold + STSG transplantation (EM), and E/C dermal scaffold + STSG transplantation (E/C). The grafts were stitched to adjacent skin with discontinuous sutures and packed on top of the graft. After surgery, each rat was housed in individual cages. On the 3rd, 7th, 14th, 28th, and 56th days after the operation, the grafts were observed and photographed, the dressings were changed regularly, and samples were taken. The graft size was measured by ImageJ software, and the relative graft sizes were calculated using the following formula

$$\text{relative skin graft size\%} = \text{remaining skin graft size/original skin graft size} \times 100$$



https://doi.org/10.1021/acsami.3c04733
ACS Appl. Mater. Interfaces 2023, 15, 38230−38246

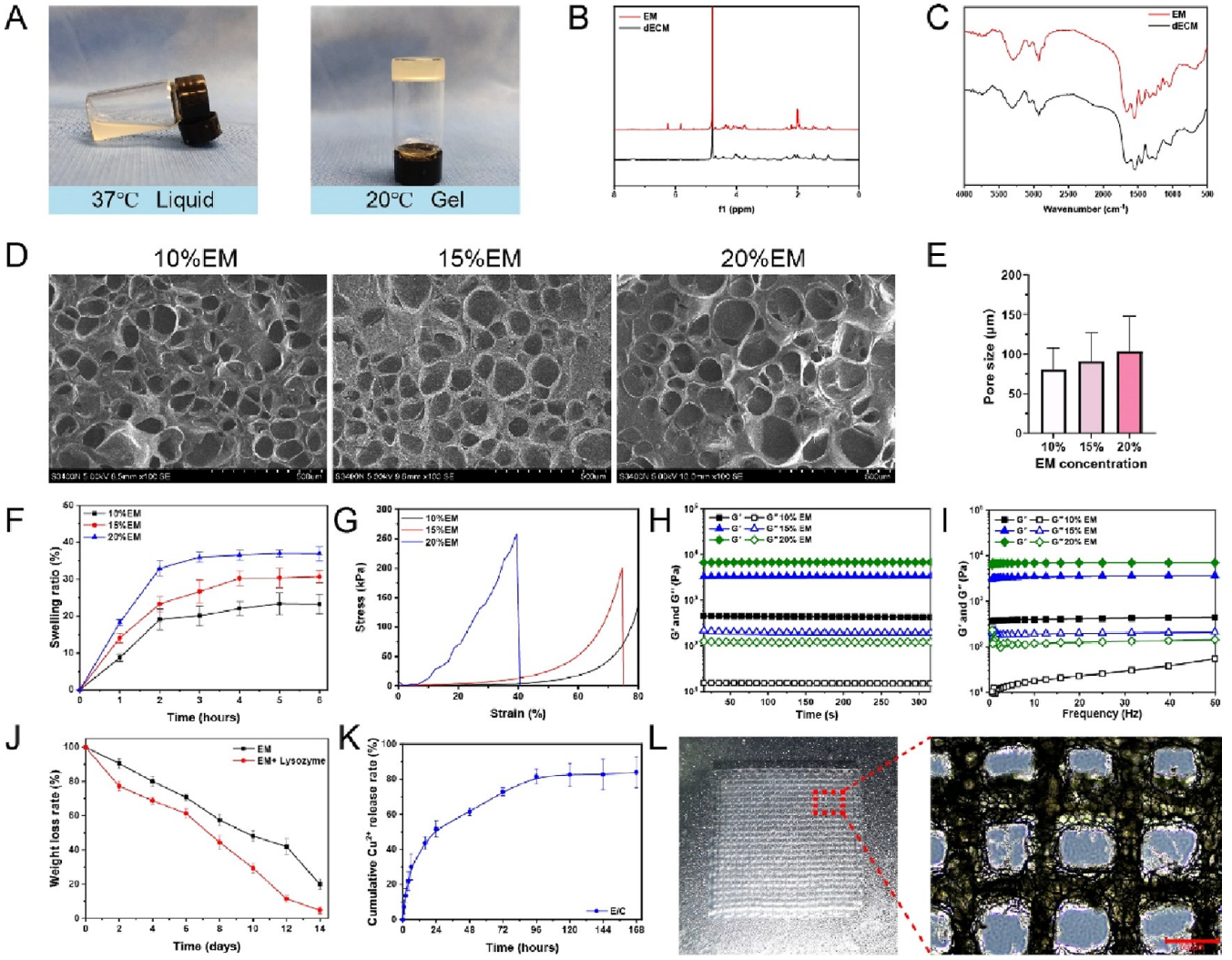


**Figure 2.** (A) Photograph of the thermosensitive bioink. (B) $^{1}$H NMR spectra of dECM and ECMMA, aka EM. (C) FTIR spectra of dECM and EM. (D) SEM images of EM hydrogels. (E) Pore size of EM hydrogels. The swelling ratio (F), stress−strain curve (G), and rheological properties (H, I) of EM hydrogels. (J) Degradation curve of EM with or without lysozyme. (K) Release curve of copper ions in the E/C hydrogel. (l) Optical photograph of the EM dermis scaffold. (M) Microscopic appearance of the EM dermis scaffold.

*2.12.2. Histological Staining.* The tissues excised from the skin-grafted area and the adjacent uninjured skin (UIS) were fixed, embedded, and cut into 5 $\mu$m thick sections. After dewaxing and rehydration, the sections were dyed with H&E staining, Masson staining, and Sirius red staining. All slides were scanned using a digital pathology scanner (KF-PRO-020, KFBIO, China) and analyzed using ImageJ software.

*2.12.3. Immunohistochemical Staining.* For antigen retrieval, dewaxed and rehydrated slides were immersed in citrate antigen retrieval buffer (Elabscience, USA). Slides were then incubated in 3% hydrogen peroxide solution in the dark for 25 min to block endogenous peroxidase, followed by incubation in 3% BSA for 30 min at room temperature to block nonspecific antigens. Subsequently, the slides were incubated with the following primary antibodies overnight at 4 °C: anti-CD31 (GB11063, Servicebio, China, rabbit, 1:200), anti-collagen I (GB11022-3, Servicebio, China, rabbit, 1:1000), anti-collagen III (GB11022-3, Servicebio, China, rabbit, 1:500), anti-CD68 (GB113109, Servicebio, China, rabbit, 1:200), anti-iNOS (GB11119, Servicebio, China, rabbit, 1:500), and anti-CD206 (ab64693, Abcam, USA, rabbit, 1:10 000). Next, the slides were washed with PBS and immersed in the corresponding HRP-conjugated goat anti-rabbit (ab205718, Abcam, USA, 1:10 000) for 50 min at room temperature. Antibody binding sites were visualized by DAB chromogen, and slides were counterstained with hematoxylin.

*2.12.4. RT-PCR and ELISA.* Total RNA was isolated from homogenized tissue. The RT-PCR procedure was as described above. Total tissue protein was extracted and protein concentrations were examined by a BCA assay kit. The TNF-a and IL-1B protein levels were detected by a rat TNF-a ELISA kit (FineTest, China, ER1393) and IL-1B ELISA kit (FineTest, China, ER1094) and were normalized to total protein concentration.

**2.13. Statistical Analysis.** All experimental data were analyzed with GraphPad Prism 7.0 and SPSS 21.0 statistical software, and the data are expressed as the mean ± standard deviation ($x \pm s$). Statistical analysis was assessed using unpaired $t$ tests. $P < 0.05$ indicated that the difference was statistically significant.

## 3. RESULTS AND DISCUSSION

**3.1. Characterization of dECM and Cu-EGCG.** We performed a series of decellularization treatments on porcine NS to prepare dECM. As shown in Figure 1A, dECM was milky white and free of epidermis and hair. The results of H&E staining showed that there were normal tissues and cells in NS, and no obvious cell structure was found in dECM samples. DAPI staining revealed nuclei with blue fluorescence in NS but no fluorescence in dECM samples. The results of Masson staining indicated that the collagen components of the ADM


https://doi.org/10.1021/acsami.3c04733
ACS Appl. Mater. Interfaces 2023, 15, 38230−38246

were retained and not denatured. The contents of GAGs and collagen in NS and dECM were quantitatively detected. Compared with NS, the relative content of collagen in dECM was 118.55 ± 1.93%, and the relative content of GAG in dECM was 77.78 ± 2.81%, consistent with the trend of previous experimental results.[29] The DNA of NS and dECM was extracted for agarose gel electrophoresis, and the results showed that the residual DNA content in dECM was 9.01 ± 3.28% (Figure 1B), which further confirmed the success of the decellularization treatment.

TEM images confirmed that Cu-EGCG presents a nanoscale microstructure with a particle size of approximately 37.9 nm (Figures 1C and S1). Copper is a necessary trace metal for the human body and plays a complex role in various biological processes such as respiration, gene regulation, antioxidant defense, and neurotransmission.[30] It basically participates in all stages of wound healing and plays an essential role in skin re-epithelialization and angiogenesis.[31] EDS confirmed the presence of copper in Cu-EGCG, accounting for 17.89% (Figure 1D).

**3.2. Characterization of the Bioink and Dermal Scaffold.** *3.2.1. Characterization of the EM Bioink.* Porcine dermis-derived dECM was modified by methacrylic anhydride to prepare the EM biological ink. As the temperature decreases from body temperature (37 °C) to room temperature (20 °C), the ECM hydrogel exhibits a temperature-induced reversible sol−gel transition (Figure 2A), which is consistent with the thermosensitive characteristics of other ECM-based hydrogels.[16,32] $^1$H NMR spectrograms showed that the spectra of EM and dECM were similar. EM had two specific peaks at 5.8 and 6.2 ppm (Figure 2B), which are attributed to methacrylic anhydride, indicating the successful grafting of methacrylic acid groups onto the ECM. We further detected the functional groups of the dECM and EM with FTIR. The hydroxyl peak at ∼3300 cm$^{-1}$ was observed on both bands. The common characteristic bands of the dECM and EM are observed at 1626 cm$^{-1}$ (amide I), 1549 cm$^{-1}$ (amide II), and 1452 cm$^{-1}$ (amide III). The bending and plane vibrations of C−N and N−H correspond to the characteristic peaks of C−O−N−H and $NH_2$ in the FTIR spectra, respectively. The FTIR spectra of the two have similar peak positions and peak heights (Figure 2C), proving that the EM and dECM components are similar.

*3.2.2. SEM and Particle Analysis of the EM Bioink.* The porous and interconnected network can promote the exchange of oxygen and nutrients, drain exudate, maintain a suitable water environment, and play an important role in tissue vascularization and nascent tissue formation.[33] SEM images showed that EM had an irregular porous network structure (Figure 2D). The average pore diameters of the 10, 15, and 20 20% EM hydrogels were 80.84 ± 26.61, 91.09 ± 35.85, and 103.48 ± 43.90 μm, respectively (Figure 2E). Increasing the concentration of the hydrogel seems to cause a minor increase in its average pore size. Nonetheless, there are no significant variations between the groups. As indicated in Figure S2, the porosity ratio of the EM hydrogel diminishes with higher concentrations, which corresponds with previous research.[34]

The pore size of the hydrogel can impact its function in biomedical applications.[33,35] Wang et al.[36] detected that the human ADM has a pore size of 131.2 ± 96.8 μm. Loh et al.[33] concluded that the pore size of materials suitable for angiogenesis and skin regeneration is 20−270 μm. It was proven that the pore size of EM was similar to that of the natural human dermal matrix and had a porous structure suitable for the corresponding biological activities of cells required for wound healing.

*3.2.3. Swelling Ratio Analysis.* The swelling ratio of the material can also be affected by pore size. As the concentration of EM increases, the swelling ratio increases. The swelling ratio of EM increased rapidly in the first 2 h and reached the maximum value and swelling equilibrium within 4 h. Finally, the swelling ratios of the 10% EM, 15% EM, and 20% EM hydrogels were stable at 23.23 ± 2.66, 30.71 ± 1.72, and 36.9 ± 1.98%, respectively (Figure 2F).

*3.2.4. Compression Test and Rheological Assessment.* An ideal artificial dermal scaffold needs to have appropriate mechanical strength and deformation resistance, which can be evaluated by the compressive modulus. The compressive modulus of 10% EM is the smallest, and it had already exceeded 80% deformation under a relatively small pressure (Figure 2G). The compressive modulus of 20% EM is the highest, which is 258 kPa, but it breaks when the deformation exceeds 40.6%. The compression modulus of 15% EM is 201 kPa, which can withstand 74% deformation and still maintain its shape, which is larger than the dermis of human skin.[27]

Referring to previous studies, the viscoelasticity of the material was used to characterize the stability of the hydrogels. The storage modulus ($G'$) of all concentrations of EM is significantly larger than the loss modulus ($G''$), which illustrates their solid elastic properties (Figure 2H). The $G''$ of EM increases with the concentration, which shows that the higher concentration of EM in this range has a higher cross-linking structure (Figure 2I). Based on the above characteristics of the EM gel, a 15% concentration of EM had an appropriate pore size, water absorption, mechanical strength, resistance to denaturation, and stability and was used to prepare 3D-printed dermal scaffolds.

*3.2.5. Degradation and Copper Ion Release Rate In Vitro.* The dermal scaffolds should also be degradable with a rate that ideally matches cell and tissue regeneration. With the gradual formation of new dermis, the dermis scaffold is gradually degraded and finally completely replaced by autologous tissue to repair trauma and function. As shown in Figure 2J, the degradation curve of EM basically maintains a constant rate of degradation, and treatment with lysozyme can significantly accelerate its degradation. After 14 days, the degradation rate of the lysozyme group was 4.88 ± 1.99%, and the degradation rate of the no-enzyme group was 19.92 ± 3.02%. An appropriate degradation rate can not only maintain the stability of the dermal scaffold but also maintain the sustained release of its components. We further used ICP−MS to detect the release behavior of copper ions in the E/C hydrogel. As shown in Figure 2K, the E/C hydrogel exhibited a rapid release of $Cu^{2+}$ in the first 24 h, reaching 51.67 ± 4.77% at 24 h. The release rate of $Cu^{2+}$ tended to be stable from the second day until the release rate reached 81.6 ± 4.17% after 5 days. The results showed that the E/C hydrogel had a good sustained-release effect on $Cu^{2+}$ and were consistent with previous studies of Cu-loaded hydrogels.[37,38] Continuous release of non-cytotoxic levels of copper ions can provide longer-lasting stimulation to surrounding cells.[38]

*3.2.6. 3D Bioprinting.* We used an extrusion bioprinter to make 15% EM into a 2 cm × 2 cm square dermal scaffold with a regular appearance (Figure 2L). Meanwhile, the internal pores of the scaffold are regular and interconnected.

**3.3. In Vitro Biocompatibility Test.** Cell proliferation experiments were used to evaluate the effect of fabricated EM


https://doi.org/10.1021/acsami.3c04733
ACS Appl. Mater. Interfaces 2023, 15, 38230−38246

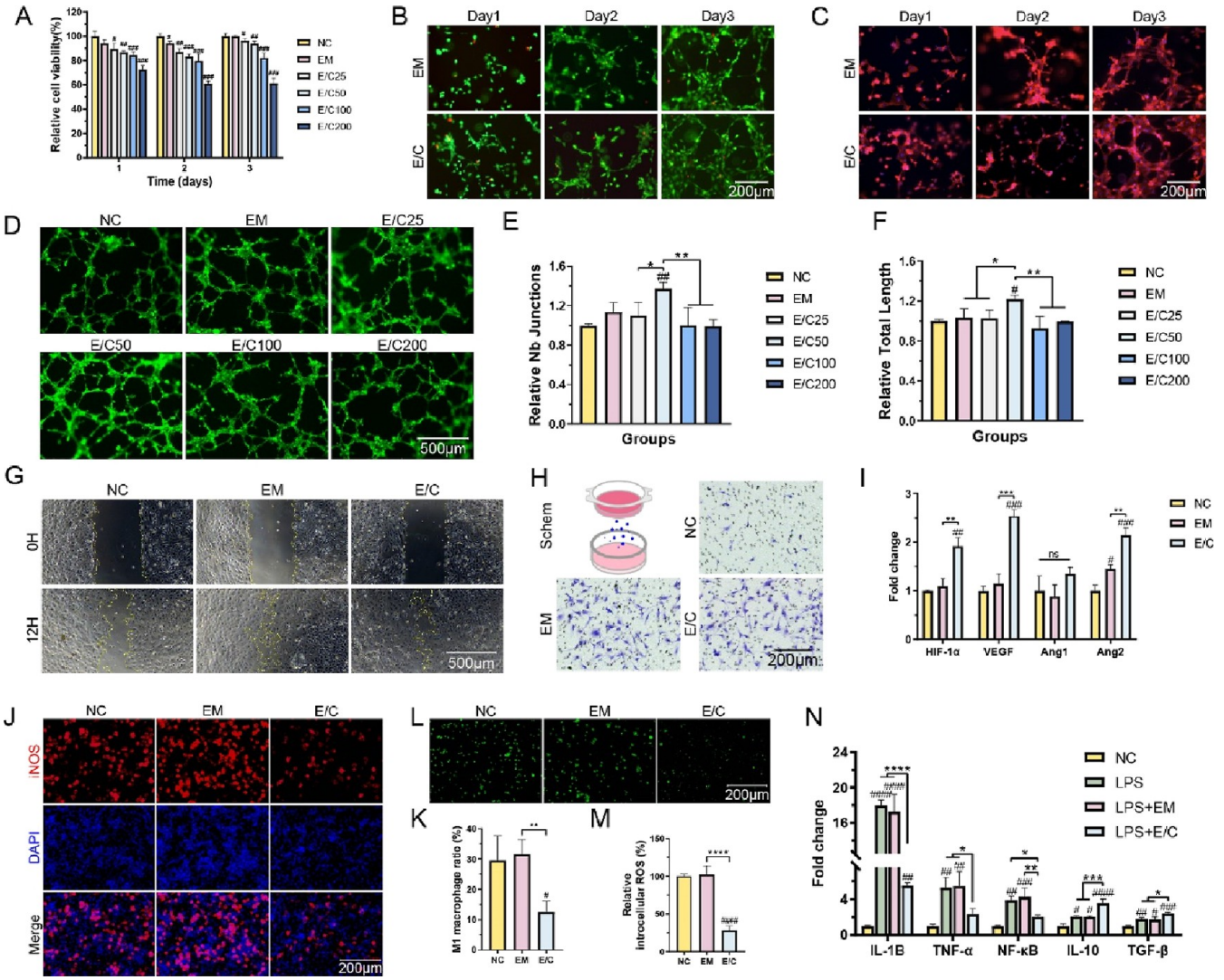


**Figure 3.** (A) Cell viability tested by CCK8 assay. (B) Live/dead staining images of HMEC-1 cells cultured on hydrogels. Viable cells: green; dead cells: red. (C) Cytoskeleton staining images of HMEC-1 cells cultured on hydrogels. (D) Fluorescence (green) images of HMEC-1 cells forming tubes in vitro. Quantitative evaluation of junctions (E) and total tube length (F) in the vascularized network structure. (G) Micrograph of the wound healing experiment. Yellow curves show the scratch area. (H) In vitro invasion assay. (I) RT-PCR analysis of ANG1 and ANG2. (J) Fluorescence graphs of M1 macrophages (iNOS+) in RAW 264.7 cells treated with LPS. (K) Quantification of M1 macrophages. (L) Fluorescence (green) graphs of intracellular ROS in RAW 264.7 macrophages after $H_2O_2$ treatment. (M) Quantification of intracellular ROS in RAW 264.7. (N) RT-PCR analysis of IL10, IL1B, NK-$\kappa$B, TNF-$\alpha$, and TGF-$\beta$. (#$P$ < 0.05, between the NC and others, ##$P$ < 0.01, ###$P$ < 0.001, ####$P$ < 0.0001. *$P$ < 0.05, between other groups, **$P$ < 0.01, ***$P$ < 0.001, ****$P$ < 0.0001).

dermal scaffolds with different concentrations of Cu-EGCG on the activity of HMEC-1 cells. The CCK-8 assay results showed that the cell viabilities after 3 days of culture in the EM, E/C25, and E/C50 groups were 100 ± 0.8, 96.3 ± 1.6, and 93.9 ± 1.9%, respectively (Figure 3A). The viabilities of HMEC-1 cells in groups E/C100 and E/C200 were 82.3 ± 3.3 and 61.1 ± 3.8%, respectively. Then, HMEC-1 cells were cultured on the gel surface for live/dead staining. As shown in Figure 3B, most of the HMEC-1 cells grown on the surface of the hydrogel survived (green fluorescence), confirming the lack of cytological toxicity of our material. As the culture continues, the HMEC-1 cells tend to grow and aggregate into a reticular structure. The reticular structure was more obvious in the cytoskeleton staining image (Figure 3C). Our results indicated that the E/C hydrogel with a concentration of Cu-EGCG less than 100 $\mu$g/mL shows minimal cytotoxicity, which is consistent with other research studies.[26,37]

**3.4. Pro-Angiogenic Effect In Vitro.** Prior studies have shown that Cu-EGCG can increase the expression of VEGF in endothelial cells and promote angiogenesis.[26] As mentioned earlier, we have determined that the release of copper ions from the E/C hydrogel reaches approximately 80% after 72 h. Therefore, a 72 h extraction from each hydrogel was used in the tube formation assay for endothelial cell culture to evaluate the pro-angiogenic effect of the E/C hydrogel. The growth of HMEC-1 cells on Matrigel is shown in Figure 3D. The statistical results showed that E/C50 significantly promoted angiogenesis better than the other treatments, $P$ < 0.05 (Figure 3E,F). E/C with 50 $\mu$g/mL Cu-EGCG had good biocompatibility and a strong ability to promote angiogenesis in vitro and was used as the optimal concentration for subsequent experiments. The statistical results showed that the tube-forming ability of HMEC-1 cells cultured on the E/C hydrogel was stronger than that of cells cultured on the EM hydrogel.


https://doi.org/10.1021/acsami.3c04733
ACS Appl. Mater. Interfaces 2023, 15, 38230−38246

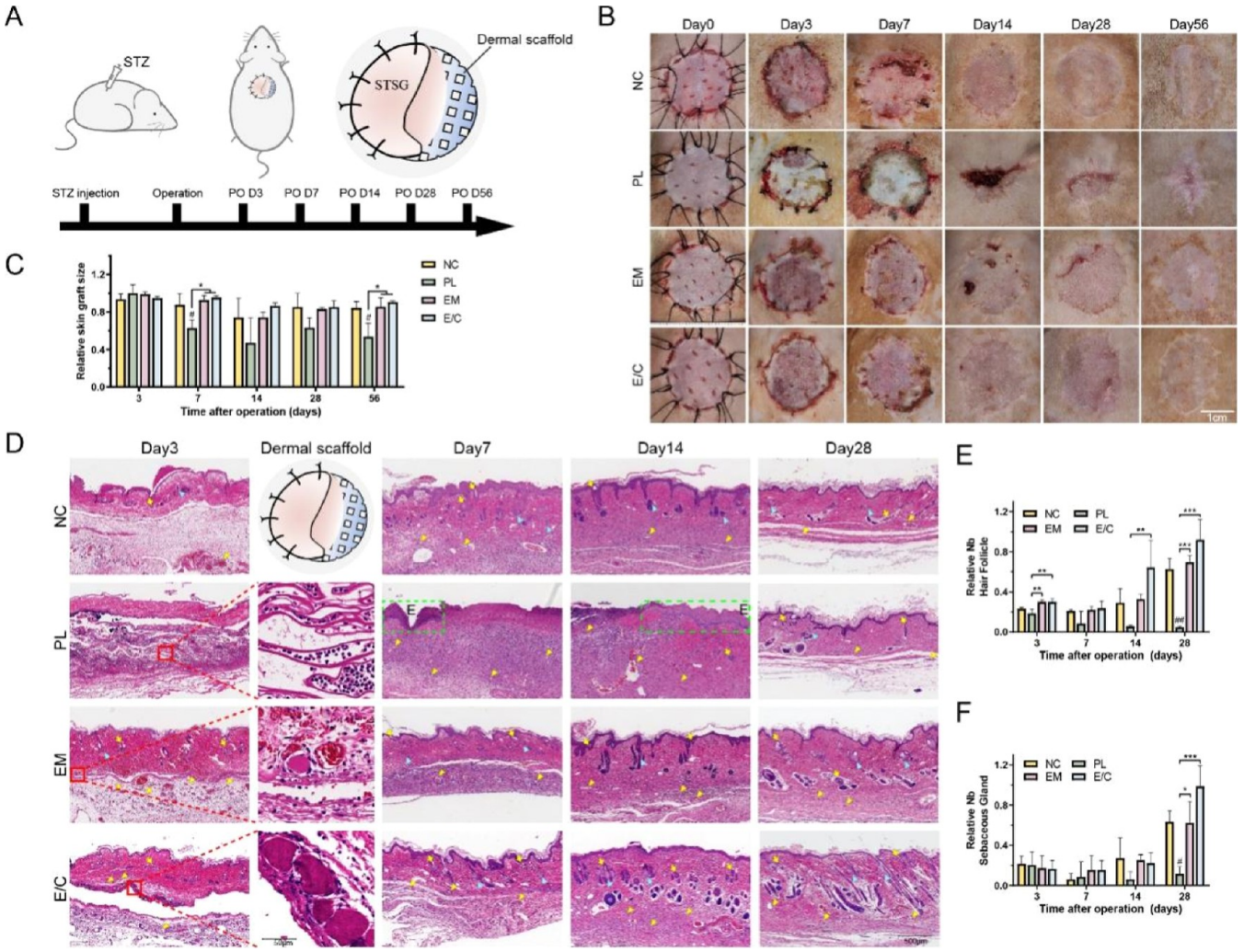


**Figure 4.** (A) Schematic of the in vivo experimental design. (B) Wound healing at 0, 3, 7, 14, 28, and 56 days after operation in different groups of diabetic rats. (C) Quantitative analysis of wound size on the 3rd, 7th, 14th, 28th, and 56th days after operation. (D) H&E staining graphs of wound sections on the 3rd, 7th, 14th, and 28th days after operation. Yellow triangle: neovascularization; yellow arrow: hair follicles; blue triangle: sebaceous glands; green dotted box: epidermis. The relative number of hair follicles (E) and sebaceous glands (F) on the 3rd, 7th, 14th, and 28th days after operation. (#$P < 0.05$, between the NC and others, ##$P < 0.01$. *$P < 0.05$, between other groups, **$P < 0.01$, ***$P < 0.001$.)

The above results confirmed that E/C hydrogels lacked cytological toxicity and may promote vascularization, which are crucial for angiogenesis and wound healing in diabetic wounds.

The migration of endothelial cells is a critical step in angiogenesis and vascular repair.[39] The migration ability of HMEC-1 cells was evaluated by an in vitro wound healing assay. The scratch gap closure rates of the EM group (75.2 ± 2.7%) and E/C50 group (79.2 ± 2.1%) were higher than that of the NC group (62.3 ± 5.6%), $P < 0.05$(Figures 3G and S3A). Invasion experiments showed that the ability to promote cell migration in the EM group and the E/C50 group was 6.6 ± 0.4 times ($P < 0.01$) and 7.0 ± 1.0 times ($P < 0.05$) that of the control group, respectively (Figures 3H and S3B). These results confirmed that both EM and E/C could promote cell migration and invasion in vitro. RT-PCR results also suggested that E/C could promote the expression of angiogenesis-related genes (HIF-1$\alpha$, VEGF, and Ang2) in HMEC-1 cells (Figure 3I).

**3.5. Anti-Inflammatory Effect In Vitro.** The inflammatory response is a necessary process for wound healing. As an important player in the inflammatory response, abnormal polarization of macrophages is an essential cause of over-digestion of tissues and delayed or even nonhealing of wounds.[40] The anti-inflammatory biological activity of Cu-EGCG has been elucidated previously.[41] As shown in Figure 3J, the anti-inflammatory effect of E/C was assessed on RAW 264.7 macrophages in vitro. 48 h after LPS-stimulated RAW 264.7 cells were cocultured with E/C, the proportion of M1 macrophages (iNOS+) was 12.47 ± 3.67%, which was significantly lower than 29.51 ± 8.09% in the NC group and 31.62 ± 4.81% in the EM group (Figure 3K), $P < 0.05$.

Macrophages could also modulate wound inflammation by regulating the oxidative stress response and secretion of inflammatory factors.[42] ROS can cause cell dysfunction and chronic inflammation at high concentrations, activate a series of inflammatory responses, induce oxidative stress, and lead to continuous inflammatory infiltration of the wound microenvironment.[43,44] Elevated ROS levels are also characteristic of diabetic wounds. Studies have shown that adding antioxidants to hydrogels can reduce oxidative stress and related cell damage.[40] The ROS level (DCFDA fluorescence intensity) in RAW 264.7 macrophages was detected. As shown in Figure 3L,


https://doi.org/10.1021/acsami.3c04733
ACS Appl. Mater. Interfaces 2023, 15, 38230−38246

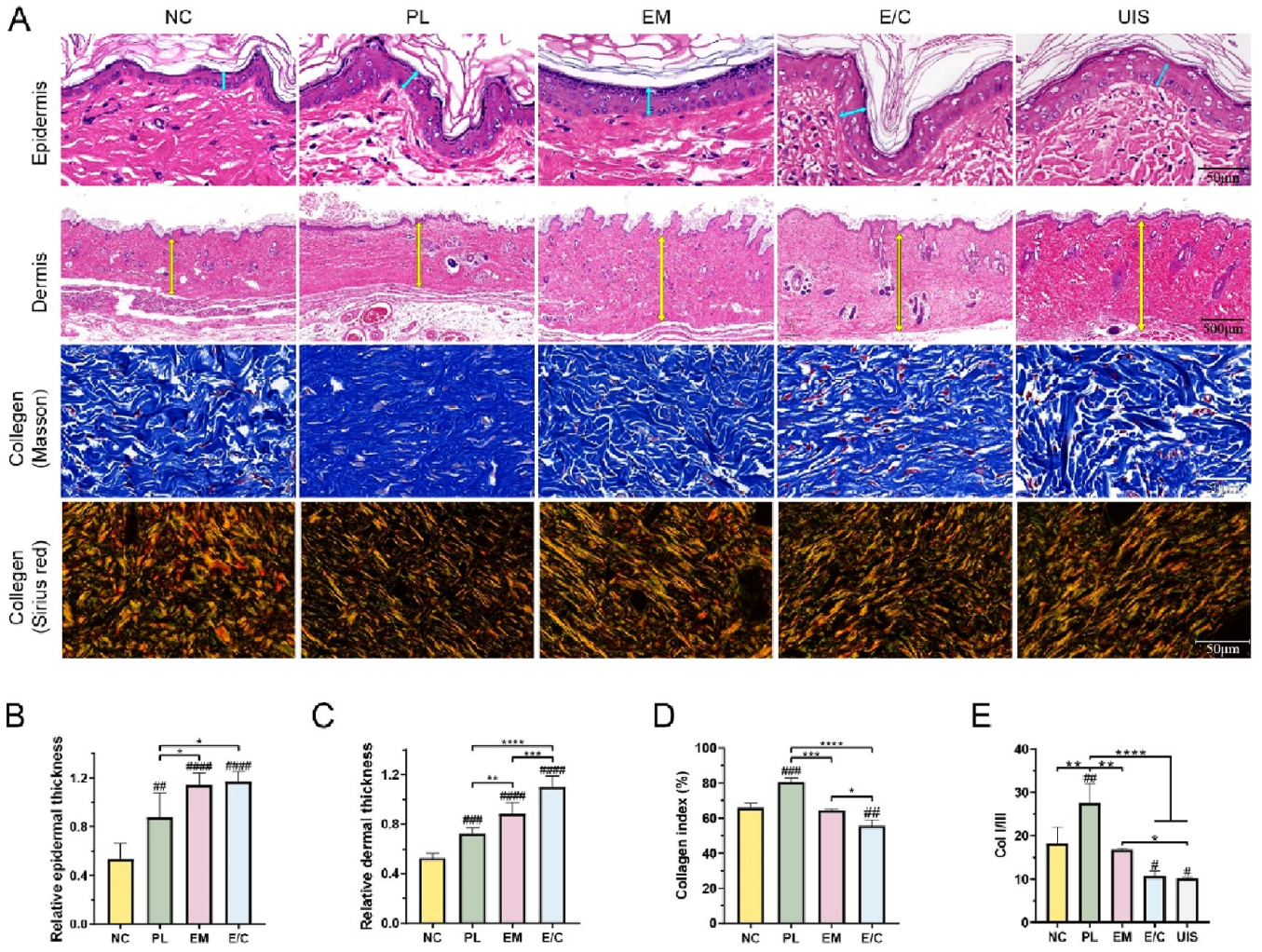


**Figure 5.** (A) H&E staining, Masson staining, and Sirius red staining images of the epidermis and dermis of each group and UIS of rats on the 56th day after operation. Quantification of the epidermis thickness (B), dermis thickness (C), collagen index (D), and ratio of Col I/III (E) of each group and UIS of rats. (#$P < 0.05$, between the NC and others, ##$P < 0.01$, ###$P < 0.001$, ####$P < 0.0001$. *$P < 0.05$, between other groups, **$P < 0.01$, ***$P < 0.001$, ****$P < 0.0001$.)

$H_2O_2$ significantly increased intracellular ROS levels. The intracellular ROS levels of macrophages cocultured with E/C dermal scaffolds were significantly lower than those in the NC and EM groups (Figure 3M). As shown in Figure 3N, the expression levels of IL-1B, NF-$\kappa$B, and TNF-$\alpha$ in RAW264.7 macrophages stimulated by LPS were higher than those in untreated RAW264.7 macrophages (NC). However, the expression of IL1B, NF-$\kappa$B, and TNF-$\alpha$ decreased significantly in the LPS + E/C group compared to the NC group, $P < 0.05$. The expression of the anti-inflammatory cytokines IL-10 and TGF-$\beta$ increased in all experimental groups, which may be caused by the negative feedback regulation of inflammation; that is, the increase in inflammatory cytokines leads to the expression of anti-inflammatory factor genes. Meanwhile, the mRNA levels of IL-10 and TGF-$\beta$ were higher in the LPS + E/C group compared to other groups, $P < 0.05$. Based on the above experimental results, it was confirmed that Cu-EGCG significantly enhanced the inflammation-modulating ability of E/C scaffolds.

**3.6. Assessment of Wound Healing in Diabetic Rats.** *3.6.1. Evaluation of Wound Healing.* A clinically equivalent, immune competent diabetic rat STSG model was used to assess the therapeutic efficacy of the E/C dermal scaffold on diabetic wounds in vivo. Pelnac (single layer), a porcine-origin commercialized implantable artificial dermis, was applied as the positive control. The surgical procedure is shown in Figure 4A. Considering the time that the morphological changes and the scar contraction of grafted wounds required to develop, the rats were followed for up to 56 days after operation.

The recovery of wounds after surgery is shown in Figure 4B. In the early postoperative period, from day 3 to day 7, the color of the STSG in the NC, EM, and E/C groups was ruddy, indicating sufficient blood supply and successful graft take. In the PL group, most of the skin grafts were pale or even festering, suggesting ischemia, degeneration, and necrosis in this area. On the 14th day after operation, the STSGs in groups NC, EM, and E/C were closely connected with the underlying wound, and the color of the grafts became similar to that of the surrounding UIS. In contrast, most of the skin grafted area in group PL produced blood scabbing due to STSG necrosis, and a few areas were re-epithelialized. In the later stage of healing (days 28−56), the skin grafts in each group gradually returned to normal skin color. In the PL group, contracture occurred, and a scar was left following STSG necrosis. The relative size of the wound area after STSG grafting in each group was counted (Figure 4C). Taking the size of the skin graft


https://doi.org/10.1021/acsami.3c04733
ACS Appl. Mater. Interfaces 2023, 15, 38230−38246

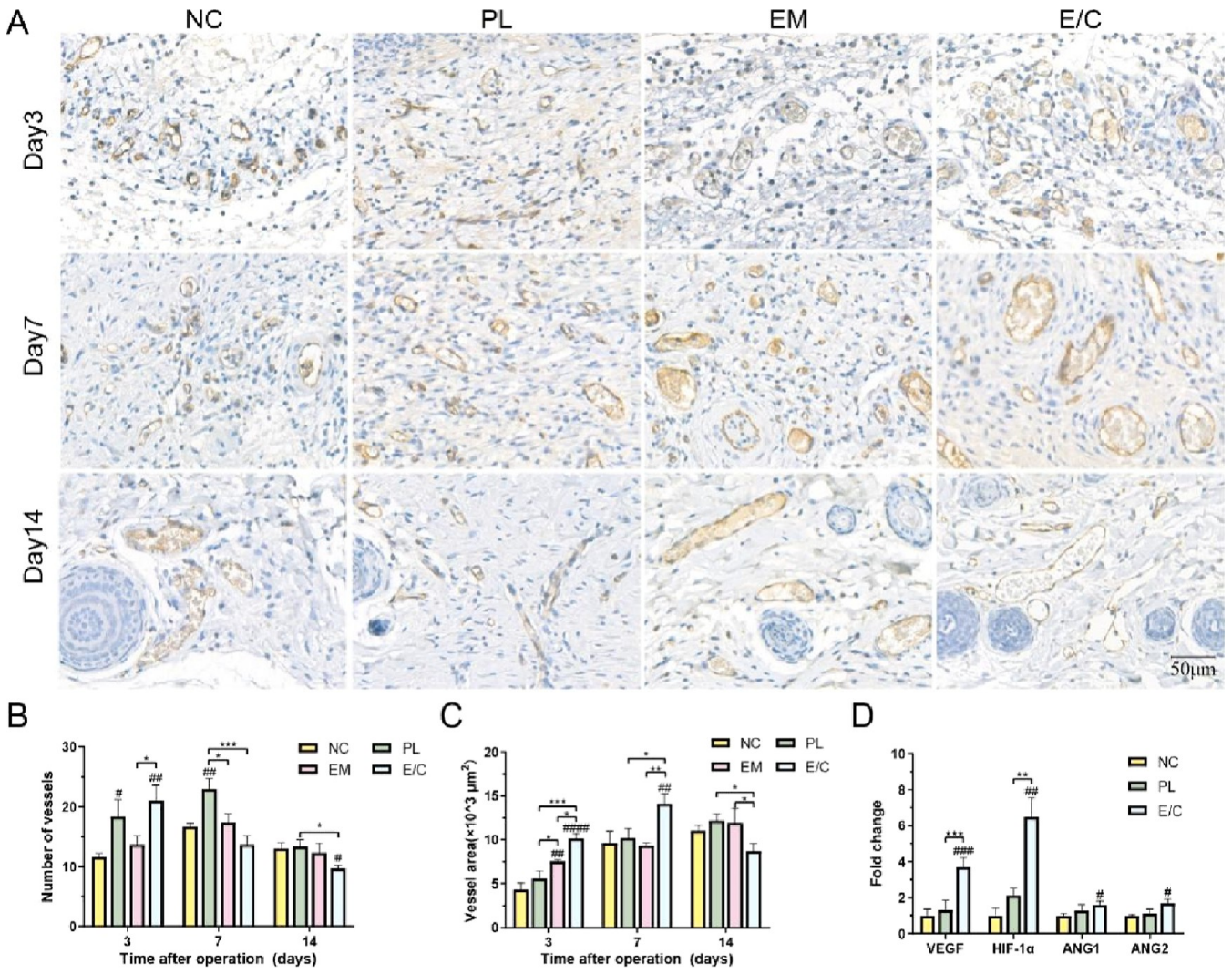


**Figure 6.** (A) CD31 immunohistochemical staining images of microvessels. Quantification of the number of microvessels (B) and microvascular area (C). (D) Fold changes in ang1, ang2, and VEGF expression in the NC, PL, and E/C groups 3 days after operation. (#$P$ < 0.05, between the NC and others, ##$P$ < 0.01, ###$P$ < 0.001, ####$P$ < 0.0001. *$P$ < 0.05, between other groups, **$P$ < 0.01, ***$P$ < 0.001.)

immediately after skin grafting as the initial area (100%), the wound size in the late healing period (56 days after operation) in group E/C was 90.76 ± 1.26%, indicating that there was no obvious contracture in rat skin after STSG transplantation. The healed wound in group PL within the late healing period was 53.60 ± 14.26%, suggesting that there was a severe contracture during the skin healing process, which was consistent with previous reports.[45,46]

Compared to foaming process-made Pelnac (i.e., its internal pores cannot be guaranteed to be fully connected), the 3D-printed E/C dermal scaffolds prepared in our study had moderate mechanical strength and all connected internal pores. The tissue fluid flows through the scaffold in the early stage after skin grafting to provide nutrients for the upper skin. Besides, for containing ECM components and equipping the well-designed physical structure, the E/C dermal scaffolds provided an in situ microenvironment for wound repair.

*3.6.2. Histological Evaluation of Wound Healing.* To further explore the effect of E/C dermal scaffolds on diabetic wound healing, we performed H&E staining of histological sections. Initial take of skin grafts was observed at 3 days after operation (Figure 4D). The implanted dermal analogues were visible under STSG. Compared with PL in which inflammatory cells were extensively infiltrated, our E/C scaffolds did not elicit a significant inflammatory infiltrate.

Hair follicles are the key source of epidermal stem cells and fibroblasts during wound healing. Sebaceous glands play an important role in establishing skin barriers, preserving skin moisture, regulating body temperature, and preventing UV damage.[47] The presence of both can reduce the formation of scars after healing.[37] Taking the UIS of diabetic rats as the control, there were only a few sebaceous glands and hair follicles in each group 3−7 days after operation, and there was no significant difference between the groups (Figure 4E,F). 14 days after operation, the number of skin appendages in the NC, EM, and E/C groups began to increase. On the 28th day after operation, the average numbers of hair follicles and sebaceous glands in group E/C was 0.92 ± 0.17 and 0.85 ± 0.14, respectively, which was closest to that of UIS. The average numbers of hair follicles and sebaceous glands in the PL group were the lowest ($P$ < 0.05), which was consistent with the characteristic of scars.

*3.6.3. Quality Assessment of Wound Healing.* For the treatment of diabetic wounds, not only should the wound be


https://doi.org/10.1021/acsami.3c04733
ACS Appl. Mater. Interfaces 2023, 15, 38230−38246

closed as soon as possible, but also the skin function should be restored as much as possible to reduce the possibility of scar healing and ulcer recurrence. To further evaluate the quality of wound healing, the thicknesses of the epidermis and dermis of the skin-grafting area in the late healing period (56 days after surgery) were analyzed (Figure 5A). There was no significant difference in the thickness of the epidermis and dermis of group E/C compared with UIS of diabetic rats (Figure 5B). The thickness of the dermis was slightly thinner in group EM (Figure 5C). Our results were consistent with previous studies showing that heterogeneous dermal scaffolds applied to deep wounds can increase the thickness of skin after wound healing.[48] The thickness of the epidermis and dermis in all groups with skin grafts of dermal scaffolds combined with STSG was thicker than that in the NC group. However, HE staining showed that some of the dermal fibers in group PL were dense and there were no skin appendages, suggesting scar formation.

The relative arrangement of the ECM of the dermis is associated with skin scarring.[49] For example, human pathological scars contain higher collagen levels but have weaker material properties than UIS because of the lack of basket-weave ECM organization. Masson staining images showed that the collagen fibers in the NC, EM, and E/C groups were arranged in a basket-weave manner, consistent with the normal dermis of rats (Figure 5A). The dermis in group PL showed dense and parallel fiber arrangements, which is consistent with hypertrophic scar features.[50] Quantitative analysis of the collagen index in dermis further supported these observations. The collagen index in the PL group (80.66 ± 1.82%) was the highest (Figure 5D). Meanwhile, the collagen index in group E/C (55.7 ± 2.7%) was similar to that in UIS (57.3 ± 3.7%). The two main collagen types in wound repair are collagen I and collagen III, the ratio of which remains constant in normal skin. But in mature scar tissue formed in post-traumatic skin, the ratio of type I collagen is higher than normal, and the ratio of collagen I/III (Col I/III) is considered an indicator of scar formation, with higher values corresponding to tissue fibrosis and increased scarring.[51−54] As shown in Figure 5E, the ratios of Col I/III in NC, PL, EM and E/C groups were 18.21 ± 3.78, 27.59 ± 4.46, 16.76 ± 0.28, and 10.72 ± 1.17, respectively. The ratio of Col I/III in the E/C group was the closest to that of UIS (10.14 ± 0.25). In conclusion, the outlook, number of skin appendages, thickness of skin, collagen index, and the ratio of Col I/III in dermis after wound healing in the E/C group were the closest to those in UIS, certifying the non-scar wound healing.

*3.6.4. Neovascularization Analysis In Vivo.* The early formation of functional neovasculature after skin grafting is of great significance to the survival of skin grafts, which can also prevent scar formation and skin contracture after wound healing.[21] Microvessels were observed in the grafted skin 3 days after operation, and the number and density of blood vessels in the dermis of each group began to stabilize 14 days after operation (Figure 6A). This trend is consistent with previous studies.[55] CD31 is a transmembrane protein expressed in the early stage of angiogenesis. The expression of CD31 can be used as an indicator of angiogenesis.[56] At the earliest time point (the 3rd day) after skin grafting, the amount of angiogenesis in group E/C (21 ± 2.16/HPF) was significantly higher than that in group NC (11.67 ± 0.47/HPF) and group EM (13.67 ± 1.25/HPF), $P < 0.05$ (Figure 6B). The vascular density in group E/C decreased from the 7th day after operation and reached its lowest value on the 14th day after operation (21 ± 2.16/HPF), which was significantly lower than that of group NC (13 ± 0.82/HPF) and group PL (13.33 ± 0.94/HPF). Meanwhile, the number of microvessels in the other groups was the highest at 7 days after operation and began to decrease at 14 days after operation.

The extent of vascularization can also be determined by the microvessel area. The area of microvessels in group E/C was also the highest (10 147.66 ± 458.80 $\mu m^2$/HPF) among all groups on the 3rd day after operation, $P < 0.05$ (Figure 6C). The microvascular area of group E/C peaked on the 7th day after operation (14 099.68 ± 940.33 $\mu m^2$/HPF) and then decreased. By the 14th day after operation, the area of blood vessels in group E/C was 8513.26 ± 945.40 $\mu m^2$/HPF, which was significantly lower than that in group NC (11 018.07 ± 511.15 $\mu m^2$/HPF) and group PL (12 016.01 ± 886.36 $\mu m^2$/HPF), $P < 0.05$.

During the normal wound healing process, the angiogenic activity initially leads to the formation of a disorganized vascular network at the injury site, with probably higher vessel numbers than UIS. As the vessel density reaches its peak, vascular remodeling occurs, characterized by the regression of the vascular network and the gradual maturation of vessels.[57] The disorganized vascular formation and abnormally high number of vessels during the remodeling phase are closely associated with the development of hypertrophic scars.[58] The number of microvessels in group PL was considerable from the 3rd to the 7th day after operation. However, the blood vessels were bizarrely shaped, and the total vascular area was not high, which may be due to abnormal angiogenesis caused by inflammatory stimulation. In conclusion, the E/M dermal scaffolds applied to full-thickness wounds in diabetic rats significantly increased wound angiogenesis in the early postoperative period. It was earlier when vascular remodeling had been completed and stable vascular structure had been formed in group E/C than in the other groups.

In order to gain insight into the possible mechanism of the excellent pro-angiogenic performance in E/C group, groups NC, PL, and E/C with obvious microvascular differences in the early postoperative period (the 3rd day after operation) were selected to detect the expression of angiogenesis genes. As shown in Figure 6D, the gene expression levels of VEGF, HIF-1$\alpha$, ANG1, and ANG2 in the E/C scaffold group were 3.72 ± 0.41 times, 6.49 ± 0.86 times, 1.59 ± 0.18 times, and 1.67 ± 0.21 times that in the NC group, respectively. In addition to the elevated gene expression of angiogenesis-related cytokines (HIF-1$\alpha$, VEGF, and ANG2) in the E/C group, there was also an increase in the gene expression of ANG1, a cytokine associated with vascular maturation. These results were consistent with the results of H&E staining and CD31 immunohistochemical staining, which indicates that the E/C dermal scaffold stimulated the intrinsic potential of endothelial cells in the wound to undergo a relatively normal process of blood vessel formation, including early-stage angiogenesis and subsequent vascular maturation. Prior studies have shown that copper ions can induce the secretion of HIF-1$\alpha$ and VEGF in cells, which can effectively promote angiogenesis.[31,59,60] In our study, the slow and constant release of copper ions from the E/C dermal scaffolds promoted the expression of HIF-1$\alpha$ and VEGF both in vitro and in vivo. This result suggested that the E/C dermal scaffolds may promote angiogenesis through the HIF-1$\alpha$/VEGF pathway, thus accelerating the repair and regeneration of diabetic wounds.


https://doi.org/10.1021/acsami.3c04733
ACS Appl. Mater. Interfaces 2023, 15, 38230−38246

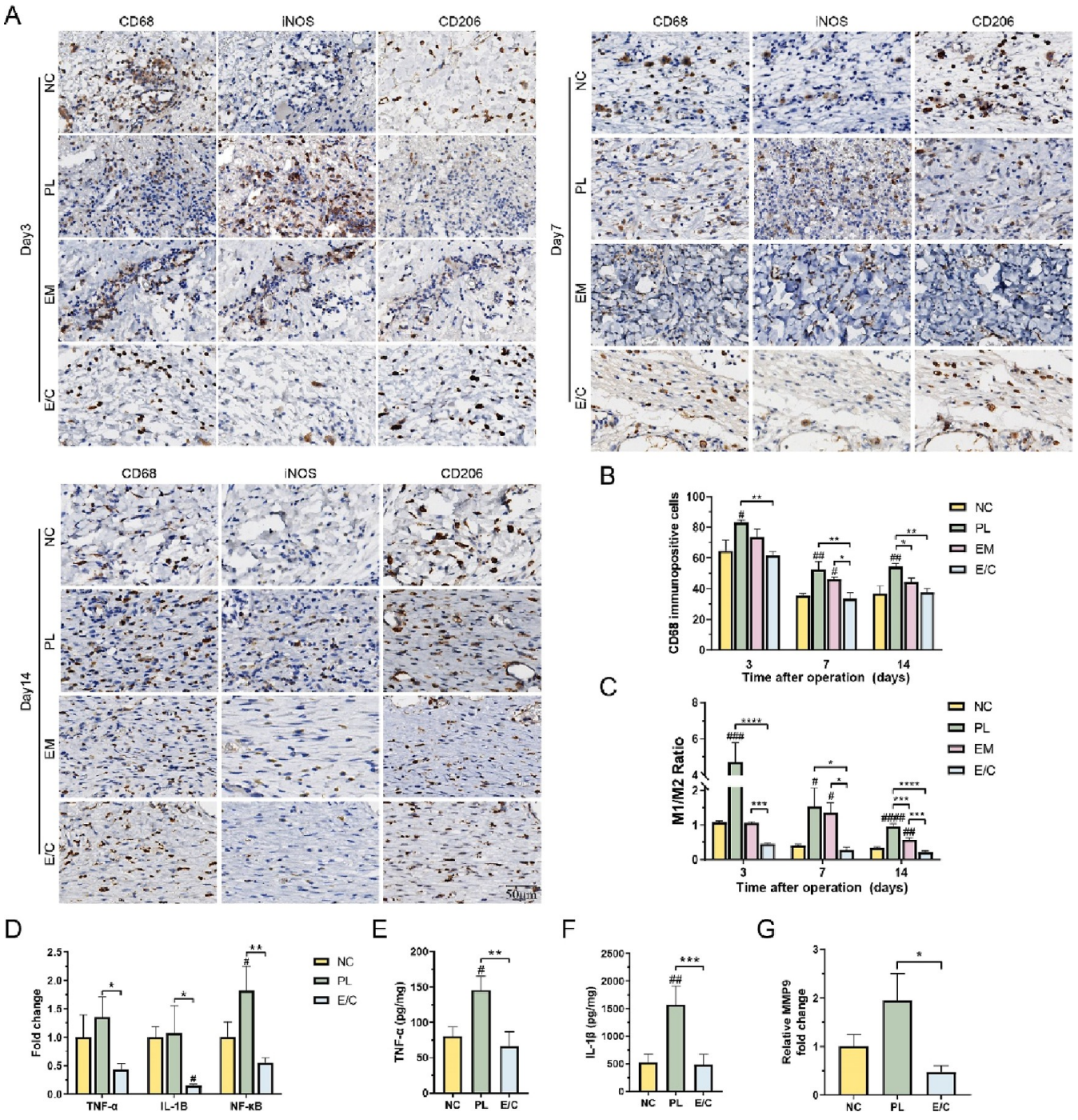


**Figure 7.** (A) Immunohistochemical staining images of the panmacrophage marker CD68, M1 macrophage marker iNOS, and M2 macrophage marker CD206. (B) Quantification of M1 macrophages. (C) Proportion of M1/M2 macrophages. (D) Fold change in the mRNA level of TNF-$\alpha$, IL-1B, and NF-$\kappa$B. TNF-$\alpha$ (E) and IL-1B (F) expression measured by ELISA. (G) Fold change in the mRNA level of MMP9. (#$P$ < 0.05, between the NC and others, ##$P$ < 0.01. *$P$ < 0.05, between other groups, **$P$ < 0.01, ***$P$ < 0.001.)

*3.6.5. Effect on Macrophage Polarization and the Inflammatory Microenvironment.* Wound healing will go through several stages of hemostasis, inflammation, proliferation, and remodeling. Diabetic ulcers have a long period of inflammation and a high level of inflammation, which prevents wounds from proceeding smoothly to the next stage and may contribute to scarring.[61] Macrophages play an important regulatory role at all stages of wound healing. Conversion of macrophages from proinflammatory M1 type to anti-inflammatory (pro-healing) M2 type is critical for normal wound repair and scar-free healing.[62,63] However, hyperglycemia hinders the transformation of macrophages from M1 to M2, keeps the wound trapped in the inflammatory phase, and impairs epithelial regeneration, collagen deposition, and angiogenesis.[44]

As shown in Figure 7A,B, the number of macrophages (CD68+) and the proportion of M1 macrophages (iNOS+) in each group were the highest at 3 days after operation. After the number of macrophages gradually decreased, the proportion of M2 macrophages (CD206+) gradually increased. This is


https://doi.org/10.1021/acsami.3c04733
ACS Appl. Mater. Interfaces 2023, 15, 38230−38246

consistent with the dynamic trend of macrophages in the wound bed in previous studies. The number of macrophages in the PL group was greater than that in the other groups, and the proportion of M1 macrophages was the highest. The number of macrophages in the NC group and the E/C group was lower than that in the other two groups, while the proportion of M1 macrophages in the E/C group was significantly lower than that in the other groups on the 3rd and 14th days after operation. On the 14th day after operation, the total number of macrophages in group E/C (39.33 ± 0.94/HPF) was the lowest among all groups, and the proportion of M2 macrophages (M1/M2 = 0.21 ± 0.04) was the highest, $P < 0.05$ (Figure 7C).

The reduction in the number of macrophages and the transformation from M1 to M2 suggested that wound healing had successfully entered the remodeling period,[62] indicating that the E/C dermal scaffolds could inhibit the inflammation of diabetic wounds and promote wound healing. A massive number of M1 macrophages that persisted in the PL group suggested that the inflammatory phase was prolonged. Previous studies have proved that dysregulated inflammation can make the wound become chronic or progressively fibrotic,[63] which is consistent with the phenomenon of impaired healing and scar formation in group PL. A moderate number of macrophages and proper proportion of M1 macrophages in the early postoperative period were seen in group E/C. The proportion of M2 macrophages in group E/C became dominant earlier than in other groups after skin plantation.

To explore the mechanism by which E/C dermal scaffolds reduce the level of inflammation in diabetic wounds, the expression of several inflammatory factors in the skin-grafting areas of the NC, PL, and E/C groups on the 3rd day after operation was detected. The mRNA levels of TNF-$\alpha$, IL-1B, and NF$\kappa$B in group E/C were the lowest, which were 0.44 ± 0.08 times, 0.16 ± 0.02 times, and 0.55 ± 0.07 times that of group NC, $P < 0.05$ (Figure 7D). The protein levels of TNF-$\alpha$ and IL-1$\beta$ were also the lowest in group E/C (Figure 7E,F). The standard curves for TNF-$\alpha$ and IL-1$\beta$ are shown in Figure S4. In diabetic ulcers, excessive inflammatory mediators can lead to changes in matrix metalloproteinase (MMP) levels in the microenvironment, resulting in excessive ECM proteolysis and wound chronicity.[62] MMPs play an important role in the normal wound remodeling process, can enzymatically dissociate tissue ECM, and mediate cell migration.[64] Excessive MMP9 can prevent wound healing. The level of MMP9 in human DFU tissue is also an important indicator of wound severity.[65] The expression of MMP9 in the E/C group was lower than that in the NC group and PL group (Figure 7G). These results are consistent with previous studies, and the level of NF-$\kappa$B p65 is positively correlated with the level of MMP9.[65]

Collectively, the E/C dermal scaffold can effectively change the phenotype of macrophages in diabetic wounds and may improve the microenvironment of diabetic wounds through the TNF-$\alpha$/NF-$\kappa$B/MMP9 pathway. Thus, it may make it earlier for the transition of diabetic wounds from the inflammatory phase to the remodeling phase and improve the quality of wound healing.

## 4. CONCLUSIONS

In this study, we prepared Cu-EGCG-loaded ECM-based 3D-printed dermal scaffolds to promote diabetic wound healing. The E/C dermal scaffolds have a good pore size distribution, appropriate physical properties, and excellent biocompatibility. These features can affect the key repair cells in the microenvironment of diabetic wounds, allowing them to exhibit expected biological activities. The scaffolds not only counteract overactive inflammatory factors and drive macrophage polarization from M1 to M2 in the wounds but also provide critical support for the aggregation and stabilization of endothelial cells into tubes. E/C dermal scaffolds enabled diabetic wounds to heal with similar skin appearance, epidermal thickness, dermal thickness, number of skin appendages, as well as the arrangement and deposition of collagen in the dermis to those of normal undamaged skin, that is, E/C dermal scaffolds reversed the scarring outcome of diabetic wounds. Overall, the E/C dermal scaffold is of great value in solving the problems of delayed wound healing and recurrence of diabetic wounds. It also provides a new insight into the clinical translation of bio-printed natural material-based products.

## ASSOCIATED CONTENT

### Supporting Information

The Supporting Information is available free of charge at https://pubs.acs.org/doi/10.1021/acsami.3c04733.

Primer information, particle size distribution of Cu-EGCG capsules, the porosity ratio of EM hydrogels, the statistical results of scratch wound-healing assays, and invasion assays (PDF)

## AUTHOR INFORMATION


### Corresponding Authors

**Lei Chen** − *Department of Burn, Wound Repair & Reconstruction, The First Affiliated Hospital of Sun Yat-Sen University, Guangzhou, Guangdong 510080, China; Guangdong Provincial Engineering Technology Research Center of Burn and Wound Accurate Diagnosis and Treatment Key Technology and Series of Products, Sun Yat-Sen University, Guangzhou, Guangdong 510080, China; Institute of Precision Medicine, The First Affiliated Hospital, Sun Yat-Sen University, Guangzhou, Guangdong 510080, China*; Email: chenlei8@mail.sysu.edu.cn

**Shaohai Qi** − *Department of Burn, Wound Repair & Reconstruction, The First Affiliated Hospital of Sun Yat-Sen University, Guangzhou, Guangdong 510080, China; Guangdong Provincial Engineering Technology Research Center of Burn and Wound Accurate Diagnosis and Treatment Key Technology and Series of Products, Sun Yat-Sen University, Guangzhou, Guangdong 510080, China; Institute of Precision Medicine, The First Affiliated Hospital, Sun Yat-Sen University, Guangzhou, Guangdong 510080, China*; Email: qishh@mail.sysu.edu.cn

### Authors

**Yanke Hu** − *Department of Burn, Wound Repair & Reconstruction, The First Affiliated Hospital of Sun Yat-Sen University, Guangzhou, Guangdong 510080, China; Guangdong Provincial Engineering Technology Research Center of Burn and Wound Accurate Diagnosis and Treatment Key Technology and Series of Products, Sun Yat-Sen University, Guangzhou, Guangdong 510080, China; Institute of Precision Medicine, The First Affiliated Hospital,*




https://doi.org/10.1021/acsami.3c04733
ACS Appl. Mater. Interfaces 2023, 15, 38230−38246

*Sun Yat-Sen University, Guangzhou, Guangdong 510080, China;* orcid.org/0000-0003-4406-9993

**Yahui Xiong** − *Department of Burn, Wound Repair & Reconstruction, The First Affiliated Hospital of Sun Yat-Sen University, Guangzhou, Guangdong 510080, China; Guangdong Provincial Engineering Technology Research Center of Burn and Wound Accurate Diagnosis and Treatment Key Technology and Series of Products, Sun Yat-Sen University, Guangzhou, Guangdong 510080, China; Institute of Precision Medicine, The First Affiliated Hospital, Sun Yat-Sen University, Guangzhou, Guangdong 510080, China*

**Yongkang Zhu** − *Department of Burn, Wound Repair & Reconstruction, The First Affiliated Hospital of Sun Yat-Sen University, Guangzhou, Guangdong 510080, China; Guangdong Provincial Engineering Technology Research Center of Burn and Wound Accurate Diagnosis and Treatment Key Technology and Series of Products, Sun Yat-Sen University, Guangzhou, Guangdong 510080, China; Institute of Precision Medicine, The First Affiliated Hospital, Sun Yat-Sen University, Guangzhou, Guangdong 510080, China*

**Fei Zhou** − *Department of Burn, Wound Repair & Reconstruction, The First Affiliated Hospital of Sun Yat-Sen University, Guangzhou, Guangdong 510080, China; Guangdong Provincial Engineering Technology Research Center of Burn and Wound Accurate Diagnosis and Treatment Key Technology and Series of Products, Sun Yat-Sen University, Guangzhou, Guangdong 510080, China; Institute of Precision Medicine, The First Affiliated Hospital, Sun Yat-Sen University, Guangzhou, Guangdong 510080, China*

**Xiaogang Liu** − *Department of Burn, Wound Repair & Reconstruction, The First Affiliated Hospital of Sun Yat-Sen University, Guangzhou, Guangdong 510080, China; Guangdong Provincial Engineering Technology Research Center of Burn and Wound Accurate Diagnosis and Treatment Key Technology and Series of Products, Sun Yat-Sen University, Guangzhou, Guangdong 510080, China; Institute of Precision Medicine, The First Affiliated Hospital, Sun Yat-Sen University, Guangzhou, Guangdong 510080, China*

**Shuying Chen** − *Department of Burn, Wound Repair & Reconstruction, The First Affiliated Hospital of Sun Yat-Sen University, Guangzhou, Guangdong 510080, China; Guangdong Provincial Engineering Technology Research Center of Burn and Wound Accurate Diagnosis and Treatment Key Technology and Series of Products, Sun Yat-Sen University, Guangzhou, Guangdong 510080, China; Institute of Precision Medicine, The First Affiliated Hospital, Sun Yat-Sen University, Guangzhou, Guangdong 510080, China*

**Zhanpeng Li** − *Department of Burn, Wound Repair & Reconstruction, The First Affiliated Hospital of Sun Yat-Sen University, Guangzhou, Guangdong 510080, China; Guangdong Provincial Engineering Technology Research Center of Burn and Wound Accurate Diagnosis and Treatment Key Technology and Series of Products, Sun Yat-Sen University, Guangzhou, Guangdong 510080, China; Institute of Precision Medicine, The First Affiliated Hospital, Sun Yat-Sen University, Guangzhou, Guangdong 510080, China*

Complete contact information is available at: https://pubs.acs.org/10.1021/acsami.3c04733

### Author Contributions

[‖]These authors contributed equally to this work.

### Notes

The authors declare no competing financial interest.

## ■ ACKNOWLEDGMENTS

This work was financially supported by the Guangdong Basic and Applied Basic Research Foundation (2020B1515020049).

## ■ ABBREVIATIONS

Cu-EGCG, copper-epigallocatechin gallate
ECMMA (EM), methacrylated decellularized extracellular matrix
E/C, EM/Cu-EGCG
STSG, split-thickness skin graft
DFUs, diabetic foot ulcers
ECM, extracellular matrix
ADM, acellular dermal matrix
dECM, decellularized extracellular matrix
VEGF, vascular endothelial growth factor
EDTA, ethylene diamine tetraacetic acid
H&E, hematoxylin and eosin
GAG, glycosaminoglycan
PSS, poly(sodium 4-styrenesulfonate)
MOPS, 3-(*N*-morpholino)propanesulfonic acid
TEM, transmission electron microscopy
EDS, energy-dispersive X-ray spectroscopy
GMA, glycidyl methacrylate
$^{1}$H NMR, $^{1}$H nuclear magnetic resonance spectroscopy
SEM, scanning electron microscopy
ICP−AES, inductively coupled plasma atomic emission spectroscopy
DCFDA, 2′,7′-dichlorodihydrofluorescein diacetate
RT-PCR, real-time polymerase chain reaction
STZ, streptozotocin
UIS, uninjured skin

## ■ REFERENCES

(1) Zhang, C.; Merana, G. R.; Harris-Tryon, T.; Scharschmidt, T. C. Skin Immunity: Dissecting the Complex Biology of Our Body's Outer Barrier. *Mucosal Immunol.* **2022**, *15*, 551−561.

(2) Falanga, V.; Isseroff, R. R.; Soulika, A. M.; Romanelli, M.; Margolis, D.; Kapp, S.; Granick, M.; Harding, K. Chronic Wounds. *Nat. Rev. Dis. Primers* **2022**, *8*, 50.

(3) Sun, H.; Saeedi, P.; Karuranga, S.; Pinkepank, M.; Ogurtsova, K.; Duncan, B. B.; Stein, C.; Basit, A.; Chan, J. C. N.; Mbanya, J. C.; Pavkov, M. E.; Ramachandaran, A.; Wild, S. H.; James, S.; Herman, W. H.; Zhang, P.; Bommer, C.; Kuo, S.; Boyko, E. J.; Magliano, D. J. IDF Diabetes Atlas: Global, Regional and Country-Level Diabetes Prevalence Estimates for 2021 and Projections for 2045. *Diabetes Res. Clin. Pract.* **2022**, *183*, 109119.

(4) Singh, N.; Armstrong, D. G.; Lipsky, B. A. Preventing Foot Ulcers in Patients with Diabetes. *JAMA* **2005**, *293*, 217−228.

(5) Huang, Y.; Kyriakides, T. R. The Role of Extracellular Matrix in the Pathophysiology of Diabetic Wounds. *Matrix Biol. Plus* **2020**, *6*−*7*, 100037.

(6) Maione, A. G.; Smith, A.; Kashpur, O.; Yanez, V.; Knight, E.; Mooney, D. J.; Veves, A.; Tomic-Canic, M.; Garlick, J. A. Altered ECM Deposition by Diabetic Foot Ulcer-Derived Fibroblasts Implicates Fibronectin in Chronic Wound Repair. *Wound Repair Regen.* **2016**, *24*, 630−643.

(7) Li, M.; Hou, Q.; Zhong, L.; Zhao, Y.; Fu, X. Macrophage Related Chronic Inflammation in Non-Healing Wounds. *Front. Immunol.* **2021**, *12*, 681710.
(8) Yammine, K.; Hayek, F.; Assi, C. A Meta-Analysis of Mortality after Minor Amputation among Patients with Diabetes and/or Peripheral Vascular Disease. *J. Vasc. Surg.* **2020**, *72*, 2197−2207.
(9) Rice, J. B.; Desai, U.; Cummings, A. K.; Birnbaum, H. G.; Skornicki, M.; Parsons, N. B. Burden of Diabetic Foot Ulcers for Medicare and Private Insurers. *Diabetes Care* **2014**, *37*, 651−658.
(10) Schaper, N. C. Lessons from Eurodiale. *Diabetes/Metab. Res. Rev.* **2012**, *28*, 21−26.
(11) Guo, X.; Mu, D.; Gao, F. Efficacy and Safety of Acellular Dermal Matrix in Diabetic Foot Ulcer Treatment: A Systematic Review and Meta-Analysis. *Int. J. Surg.* **2017**, *40*, 1−7.
(12) Wen, Q.; Mithieux, S. M.; Weiss, A. S. Elastin Biomaterials in Dermal Repair. *Trends Biotechnol.* **2020**, *38*, 280−291.
(13) Grier, W. K.; Tiffany, A. S.; Ramsey, M. D.; Harley, B. A. C. Incorporating B-Cyclodextrin into Collagen Scaffolds to Sequester Growth Factors and Modulate Mesenchymal Stem Cell Activity. *Acta Biomater.* **2018**, *76*, 116−125.
(14) Shang, F.; Hou, Q. Effects of Allogenic Acellular Dermal Matrix Combined with Autologous Razor-Thin Graft on Hand Appearance and Function of Patients with Extensive Burn Combined with Deep Hand Burn. *Int. Wound J.* **2021**, *18*, 279−286.
(15) Frueh, F. S.; Sanchez-Macedo, N.; Calcagni, M.; Giovanoli, P.; Lindenblatt, N. The Crucial Role of Vascularization and Lymphangiogenesis in Skin Reconstruction. *Eur. Surg. Res.* **2018**, *59*, 242−254.
(16) Kim, B. S.; Kwon, Y. W.; Kong, J. S.; Park, G. T.; Gao, G.; Han, W.; Kim, M. B.; Lee, H.; Kim, J. H.; Cho, D. W. 3d Cell Printing of in Vitro Stabilized Skin Model and in Vivo Pre-Vascularized Skin Patch Using Tissue-Specific Extracellular Matrix Bioink: A Step Towards Advanced Skin Tissue Engineering. *Biomaterials* **2018**, *168*, 38−53.
(17) Wollina, U.; Berger, U.; Mahrle, G. Immunohistochemistry of Porcine Skin. *Acta Histochem.* **1991**, *90*, 87−91.
(18) Zhang, J.; Wehrle, E.; Rubert, M.; Müller, R. 3d Bioprinting of Human Tissues: Biofabrication, Bioinks, and Bioreactors. *Int. J. Mol. Sci.* **2021**, *22*, 3971.
(19) Tan, S. H.; Ngo, Z. H.; Sci, D. B.; Leavesley, D.; Liang, K. Recent Advances in the Design of Three-Dimensional and Bioprinted Scaffolds for Full-Thickness Wound Healing. *Tissue Eng., Part B* **2022**, *28*, 160−181.
(20) Girardeau-Hubert, S.; Lynch, B.; Zuttion, F.; Label, R.; Rayee, C.; Brizion, S.; Ricois, S.; Martinez, A.; Park, E.; Kim, C.; Marinho, P. A.; Shim, J.-H.; Jin, S.; Rielland, M.; Soeur, J. Impact of Microstructure on Cell Behavior and Tissue Mechanics in Collagen and Dermal Decellularized Extra-Cellular Matrices. *Acta Biomater.* **2022**, *143*, 100−114.
(21) Chen, L.; Li, Z.; Zheng, Y.; Zhou, F.; Zhao, J.; Zhai, Q.; Zhang, Z.; Liu, T.; Chen, Y.; Qi, S. 3d-Printed Dermis-Specific Extracellular Matrix Mitigates Scar Contraction Via Inducing Early Angiogenesis and Macrophage M2 Polarization. *Bioact. Mater.* **2022**, *10*, 236−246.
(22) Huang, H. T.; Cheng, T. L.; Yang, C. D.; Chang, C. F.; Ho, C. J.; Chuang, S. C.; Li, J. Y.; Huang, S. H.; Lin, Y. S.; Shen, H. Y.; Yu, T. H.; Kang, L.; Lin, S. Y.; Chen, C. H. Intra-Articular Injection of (-)-Epigallocatechin 3-Gallate (Egcg) Ameliorates Cartilage Degeneration in Guinea Pigs with Spontaneous Osteoarthritis. *Antioxidants* **2021**, *10*, 178.
(23) Schilrreff, P.; Alexiev, U. Chronic Inflammation in Non-Healing Skin Wounds and Promising Natural Bioactive Compounds Treatment. *Int. J. Mol. Sci.* **2022**, *23*, 4928.
(24) Sun, M.; Xie, Q.; Cai, X.; Liu, Z.; Wang, Y.; Dong, X.; Xu, Y. Preparation and Characterization of Epigallocatechin Gallate, Ascorbic Acid, Gelatin, Chitosan Nanoparticles and Their Beneficial Effect on Wound Healing of Diabetic Mice. *Int. J. Biol. Macromol.* **2020**, *148*, 777−784.
(25) Guo, Y.; Sun, Q.; Wu, F. G.; Dai, Y.; Chen, X. Polyphenol-Containing Nanoparticles: Synthesis, Properties, and Therapeutic Delivery. *Adv. Mater.* **2021**, *33*, No. e2007356.
(26) Duan, J.; Chen, Z.; Liang, X.; Chen, Y.; Li, H.; Tian, X.; Zhang, M.; Wang, X.; Sun, H.; Kong, D.; Li, Y.; Yang, J. Construction and Application of Therapeutic Metal-Polyphenol Capsule for Peripheral Artery Disease. *Biomaterials* **2020**, *255*, 120199.
(27) Xiong, Y.; Xu, Y.; Zhou, F.; Hu, Y.; Zhao, J.; Liu, Z.; Zhai, Q.; Qi, S.; Zhang, Z.; Chen, L. Bio-Functional Hydrogel with Antibacterial and Anti-Inflammatory Dual Properties to Combat with Burn Wound Infection. *Bioeng. Transl. Med.* **2023**, *8*, No. e10373.
(28) Cui, H.; Chai, Y.; Yu, Y. Progress in Developing Decellularized Bioscaffolds for Enhancing Skin Construction. *J. Biomed. Mater. Res., Part A* **2019**, *107*, 1849−1859.
(29) Won, J. Y.; Lee, M. H.; Kim, M. J.; Min, K. H.; Ahn, G.; Han, J. S.; Jin, S.; Yun, W. S.; Shim, J. H. A Potential Dermal Substitute Using Decellularized Dermis Extracellular Matrix Derived Bio-Ink. *Artif. Cells, Nanomed., Biotechnol.* **2019**, *47*, 644−649.
(30) Kornblatt, A. P.; Nicoletti, V. G.; Travaglia, A. The Neglected Role of Copper Ions in Wound Healing. *J. Inorg. Biochem.* **2016**, *161*, 1−8.
(31) Salvo, J.; Sandoval, C. Role of Copper Nanoparticles in Wound Healing for Chronic Wounds: Literature Review. *Burns Trauma* **2022**, *10*, tkab047.
(32) Xing, H.; Zhang, Z.; Mao, Q.; Wang, C.; Zhou, Y.; Zhou, X.; Ying, L.; Xu, H.; Hu, S.; Zhang, N. Injectable Exosome-Functionalized Extracellular Matrix Hydrogel for Metabolism Balance and Pyroptosis Regulation in Intervertebral Disc Degeneration. *J. Nanobiotechnol.* **2021**, *19*, 264.
(33) Loh, Q. L.; Choong, C. Three-Dimensional Scaffolds for Tissue Engineering Applications: Role of Porosity and Pore Size. *Tissue Eng., Part B* **2013**, *19*, 485−502.
(34) Kopp, A.; Smeets, R.; Gosau, M.; Friedrich, R. E.; Fuest, S.; Behbahani, M.; Barbeck, M.; Rutkowski, R.; Burg, S.; Kluwe, L.; Henningsen, A. Production and Characterization of Porous Fibroin Scaffolds for Regenerative Medical Application. *In Vivo* **2019**, *33*, 757−762.
(35) Cao, H.; Duan, L.; Zhang, Y.; Cao, J.; Zhang, K. Current Hydrogel Advances in Physicochemical and Biological Response-Driven Biomedical Application Diversity. *Signal Transduction Targeted Ther.* **2021**, *6*, 426.
(36) Wang, Y.; Xu, R.; Luo, G.; Lei, Q.; Shu, Q.; Yao, Z.; Li, H.; Zhou, J.; Tan, J.; Yang, S.; Zhan, R.; He, W.; Wu, J. Biomimetic Fibroblast-Loaded Artificial Dermis with "Sandwich" Structure and Designed Gradient Pore Sizes Promotes Wound Healing by Favoring Granulation Tissue Formation and Wound Re-Epithelialization. *Acta Biomater.* **2016**, *30*, 246−257.
(37) Liu, N.; Zhu, S.; Deng, Y.; Xie, M.; Zhao, M.; Sun, T.; Yu, C.; Zhong, Y.; Guo, R.; Cheng, K.; Chang, D.; Zhu, P. Construction of Multifunctional Hydrogel with Metal-Polyphenol Capsules for Infected Full-Thickness Skin Wound Healing. *Bioact. Mater.* **2023**, *24*, 69−80.
(38) Xiao, J.; Chen, S.; Yi, J.; Zhang, H.; Ameer, G. A. A Cooperative Copper Metal-Organic Framework-Hydrogel System Improves Wound Healing in Diabetes. *Adv. Funct. Mater.* **2017**, *27*, 1604872.
(39) Bi, H.; Li, H.; Zhang, C.; Mao, Y.; Nie, F.; Xing, Y.; Sha, W.; Wang, X.; Irwin, D. M.; Tan, H. Stromal Vascular Fraction Promotes Migration of Fibroblasts and Angiogenesis through Regulation of Extracellular Matrix in the Skin Wound Healing Process. *Stem Cell Res. Ther.* **2019**, *10*, 302.
(40) Qian, Y.; Zheng, Y.; Jin, J.; Wu, X.; Xu, K.; Dai, M.; Niu, Q.; Zheng, H.; He, X.; Shen, J. Immunoregulation in Diabetic Wound Repair with a Photoenhanced Glycyrrhizic Acid Hydrogel Scaffold. *Adv. Mater.* **2022**, *34*, 2200521.
(41) Li, A.; Li, L.; Zhao, B.; Li, X.; Liang, W.; Lang, M.; Cheng, B.; Li, J. Antibacterial, Antioxidant and Anti-Inflammatory Plcl/Gelatin Nanofiber Membranes to Promote Wound Healing. *Int. J. Biol. Macromol.* **2022**, *194*, 914−923.
(42) Louiselle, A. E.; Niemiec, S. M.; Zgheib, C.; Liechty, K. W. Macrophage Polarization and Diabetic Wound Healing. *Transl. Res.* **2021**, *236*, 109−116.


https://doi.org/10.1021/acsami.3c04733
ACS Appl. Mater. Interfaces 2023, 15, 38230−38246

(43) Amirsadeghi, A.; Jafari, A.; Eggermont, L. J.; Hashemi, S. S.; Bencherif, S. A.; Khorram, M. Vascularization Strategies for Skin Tissue Engineering. *Biomater. Sci.* **2020**, *8*, 4073−4094.
(44) Huang, C.; Dong, L.; Zhao, B.; Lu, Y.; Huang, S.; Yuan, Z.; Luo, G.; Xu, Y.; Qian, W. Anti-Inflammatory Hydrogel Dressings and Skin Wound Healing. *Clin. Transl. Med.* **2022**, *12*, No. e1094.
(45) Corrêa, F. B.; Castro, J. C. D.; Almeida, I. R.; Farina-Junior, J. A.; Coltro, P. S. Evaluation of Contraction of the Split-Thickness Skin Graft Using Three Dermal Matrices in the Treatment of Burn Contractures: A Randomised Clinical Trial. *Wound Repair Regen.* **2022**, *30*, 222−231.
(46) Wang, X.; Wu, P.; Hu, X.; You, C.; Guo, R.; Shi, H.; Guo, S.; Zhou, H.; Chaoheng, Y.; Zhang, Y.; Han, C. Polyurethane Membrane/Knitted Mesh-Reinforced Collagen-Chitosan Bilayer Dermal Substitute for the Repair of Full-Thickness Skin Defects Via a Two-Step Procedure. *J. Mech. Behav. Biomed. Mater.* **2016**, *56*, 120−133.
(47) Lopes-Marques, M.; Machado, A. M.; Alves, L. Q.; Fonseca, M. M.; Barbosa, S.; Sinding, M. H. S.; Rasmussen, M. H.; Iversen, M. R.; Frost Bertelsen, M.; Campos, P. F.; da Fonseca, R.; Ruivo, R.; Castro, L. F. C. Complete Inactivation of Sebum-Producing Genes Parallels the Loss of Sebaceous Glands in Cetacea. *Mol. Biol. Evol.* **2019**, *36*, 1270−1280.
(48) Ayaz, M.; Najafi, A.; Karami, M. Y. Thin Split Thickness Skin Grafting on Human Acellular Dermal Matrix Scaffold for the Treatment of Deep Burn Wounds. *Int. J. Organ Transplant. Med.* **2021**, *12*, 44−51.
(49) Mascharak, S.; desJardins-Park, H. E.; Davitt, M. F.; Griffin, M.; Borrelli, M. R.; Moore, A. L.; Chen, K.; Duoto, B.; Chinta, M.; Foster, D. S.; Shen, A. H.; Januszyk, M.; Kwon, S. H.; Wernig, G.; Wan, D. C.; Lorenz, H. P.; Gurtner, G. C.; Longaker, M. T. Preventing Engrailed-1 Activation in Fibroblasts Yields Wound Regeneration without Scarring. *Science* **2021**, *372*, No. eaba2374.
(50) Jorgensen, A. M.; Varkey, M.; Gorkun, A.; Clouse, C.; Xu, L.; Chou, Z.; Murphy, S. V.; Molnar, J.; Lee, S. J.; Yoo, J. J.; Soker, S.; Atala, A. Bioprinted Skin Recapitulates Normal Collagen Remodeling in Full-Thickness Wounds. *Tissue Eng., Part A* **2020**, *26*, 512−526.
(51) Zheng, X.; Ding, Z.; Cheng, W.; Lu, Q.; Kong, X.; Zhou, X.; Lu, G.; Kaplan, D. L. Microskin-Inspired Injectable Msc-Laden Hydrogels for Scarless Wound Healing with Hair Follicles. *Adv. Healthcare Mater.* **2020**, *9*, No. e2000041.
(52) Wolfram, D.; Tzankov, A.; Pülzl, P.; Piza-Katzer, H. Hypertrophic Scars and Keloids–a Review of Their Pathophysiology, Risk Factors, and Therapeutic Management. *Dermatol. Surg.* **2009**, *35*, 171−181.
(53) Chaudhari, N.; Findlay, A. D.; Stevenson, A. W.; Clemons, T. D.; Yao, Y.; Joshi, A.; Sayyar, S.; Wallace, G.; Rea, S.; Toshniwal, P.; Deng, Z.; Melton, P. E.; Hortin, N.; Iyer, K. S.; Jarolimek, W.; Wood, F. M.; Fear, M. W. Topical Application of an Irreversible Small Molecule Inhibitor of Lysyl Oxidases Ameliorates Skin Scarring and Fibrosis. *Nat. Commun.* **2022**, *13*, 5555.
(54) Lorden, E. R.; Miller, K. J.; Bashirov, L.; Ibrahim, M. M.; Hammett, E.; Jung, Y.; Medina, M. A.; Rastegarpour, A.; Selim, M. A.; Leong, K. W.; Levinson, H. Mitigation of Hypertrophic Scar Contraction Via an Elastomeric Biodegradable Scaffold. *Biomaterials* **2015**, *43*, 61−70.
(55) Reiffel, A. J.; Henderson, P. W.; Krijgh, D. D.; Belkin, D. A.; Zheng, Y.; Bonassar, L. J.; Stroock, A. D.; Spector, J. A. Mathematical Modeling and Frequency Gradient Analysis of Cellular and Vascular Invasion into Integra and Strattice: Toward Optimal Design of Tissue Regeneration Scaffolds. *Plast. Reconstr. Surg.* **2012**, *129*, 89−99.
(56) Tan, Z.; Zhou, B.; Zheng, J.; Huang, Y.; Zeng, H.; Xue, L.; Wang, D. Lithium and Copper Induce the Osteogenesis-Angiogenesis Coupling of Bone Marrow Mesenchymal Stem Cells Via Crosstalk between Canonical Wnt and Hif-1$\alpha$ Signaling Pathways. *Stem Cells Int.* **2021**, *2021*, 6662164.
(57) Urciuolo, F.; Casale, C.; Imparato, G.; Netti, P. A. Bioengineered Skin Substitutes: The Role of Extracellular Matrix and Vascularization in the Healing of Deep Wounds. *J. Clin. Med.* **2019**, *8*, 2083.
(58) Yuan, B.; Upton, Z.; Leavesley, D.; Fan, C.; Wang, X. Q. Vascular and Collagen Target: A Rational Approach to Hypertrophic Scar Management. *Adv. Wound Care* **2023**, *12*, 38−55.
(59) Ryan, E. J.; Ryan, A. J.; González-Vázquez, A.; Philippart, A.; Ciraldo, F. E.; Hobbs, C.; Nicolosi, V.; Boccaccini, A. R.; Kearney, C. J.; O'Brien, F. J. Collagen Scaffolds Functionalised with Copper-Eluting Bioactive Glass Reduce Infection and Enhance Osteogenesis and Angiogenesis Both in Vitro and in Vivo. *Biomaterials* **2019**, *197*, 405−416.
(60) Li, Y.; Xu, T.; Tu, Z.; Dai, W.; Xue, Y.; Tang, C.; Gao, W.; Mao, C.; Lei, B.; Lin, C. Bioactive Antibacterial Silica-Based Nanocomposites Hydrogel Scaffolds with High Angiogenesis for Promoting Diabetic Wound Healing and Skin Repair. *Theranostics* **2020**, *10*, 4929−4943.
(61) Wang, Z. C.; Zhao, W. Y.; Cao, Y.; Liu, Y. Q.; Sun, Q.; Shi, P.; Cai, J. Q.; Shen, X. Z.; Tan, W. Q. The Roles of Inflammation in Keloid and Hypertrophic Scars. *Front. Immunol.* **2020**, *11*, 603187.
(62) Hesketh, M.; Sahin, K. B.; West, Z. E.; Murray, R. Z. Macrophage Phenotypes Regulate Scar Formation and Chronic Wound Healing. *Int. J. Mol. Sci.* **2017**, *18*, 1545.
(63) Eming, S. A.; Wynn, T. A.; Martin, P. Inflammation and Metabolism in Tissue Repair and Regeneration. *Science* **2017**, *356*, 1026−1030.
(64) Dai, J.; Shen, J.; Chai, Y.; Chen, H. Il-1$\beta$ Impaired Diabetic Wound Healing by Regulating Mmp-2 and Mmp-9 through the P38 Pathway. *Mediators Inflammation* **2021**, *2021*, 1−10.
(65) Chang, M.; Nguyen, T. T. Strategy for Treatment of Infected Diabetic Foot Ulcers. *Acc. Chem. Res.* **2021**, *54*, 1080−1093.


https://doi.org/10.1021/acsami.3c04733
*ACS Appl. Mater. Interfaces* 2023, 15, 38230−38246